The Beauty of Fractions

Kinematic Effects on the Sensitivity of $B_c^+ \to \tau^+ \nu_\tau$ at the LHCb

by

Charlotte A. de Wit

A DISSERTATION SUBMITTED IN PARTIAL FULFILLMENT
OF THE REQUIREMENTS FOR THE DEGREE OF

BACHELOR OF SCIENCE
PHYSICS
UNIVERSITY OF GRONINGEN

JULY, 2022

Contents

For my family because you believed in me even when I didn't.

Acknowledgments

This project was my first experience in Particle Physics research, and I could not be more appreciative of the opportunity. Throughout my Physics Bachelor's, I was not always sure what research area I might enjoy. Doing my project here has shown me that this is where my passion lies.

Kristof, thank you for your guidance and a fresh perspective when I was stuck tumbling through the order of operations rabbit hole. Your insights were incredibly helpful in helping me think about my problems from a logical perspective. This is a skill I will carry into my future studies.

MD, you were a constant source of knowledge and support. Our many conversations over various topics helped strengthen my ability, and your support helped me become more confident in communicating my results.

Pietro, thank you for going through this journey of learning with me. During the beginning of our projects, we spent a lot of time being confused together, but throughout the process, you were there to try and answer questions when I had them. We laughed and learned a lot together, and I couldn't have asked for a better friend to go through this process with.

Finally, Mick, thank you for being my supervisor and helping me throughout my journey. From the very start, I was utterly lost in particle physics, branching, and production fractions, but you were there to support and help me learn. We spent countless hours working through topics and having back-and-forth discussions that helped me find the answers when I was too blind to see them myself.

1 Introduction

Throughout our childhood, many of us are told to believe in a piece of information under the guise that the background knowledge is still too difficult for us to understand. We are taught that there is nothing smaller than protons and neutrons when there exists an entire world of magic and mystery beyond them; the world of particle physics.

The Standard Model (SM) was developed through the latter half of the 20^{th} century. It acts as a framework to describe the fundamental forces, excluding gravity, and classify the elementary particles. The SM describes two types of particles, fermions and bosons, which are classified based on an intrinsic feature called spin. Within the fermion, classification exists the leptons, electron (e), muon (μ), and tau (τ), and the quarks, up (u), down (d), strange (s), charm (c), bottom (b), and top (t).

A distinguishing property of the Standard Model is that the different leptons have the same interaction strengths, known as lepton flavour universality. A resulting consequence is that, in decays of b-hadrons, leptons should be produced at similar rates. However, upon investigating the branching fractions of B decays, B-factories Belle and Babar and the Large Hadron Collider beauty experiment (LCHb) have found values that deviate from the Standard Model's predictions. A potent approach to test lepton flavour universality is the examination of $b \to cl\nu$ transitions, with many theories outside of the SM predicting the emergence of additional particles to explain this discrepancy. To better understand this phenomenon, the branching fraction of the $B_c^+ \to \tau^+(\pi^+\pi^+\pi^-\overline{\nu_\tau})\nu_\tau$ decay * is studied, as a measurement thereof could potentially lead to new observations on lepton flavour universality.

To study lepton flavour universality, using the B_c^+ decay as a probe, b-hadrons need to be produced. This requires the use of an electron-positron or hadron collider. Electron-positron colliders are less affected by large backgrounds than hadron colliders; however, the production cross-section of b-hadrons is

*The charge conjugation transformation replaces all particles with their antiparticles without affecting the particle's position or the variables that describe its motion. Within the context of this research, charge conjugation of decay modes is implied.

Figure 1.1: The Large Hadron Collider beauty experiment at CERN. Figure from [1].

much more significant at hadron colliders. Hadron colliders benefit from larger signal generation, which is thus an asset if the backgrounds can be sufficiently rejected.

The Large Hadron Collider (LHC) is the world's largest and most powerful particle accelerator. It boasts a 27 km ring consisting of superconducting magnets and accelerating structures, increasing the particles' energy along the track. One of the main LHC experiments is the Large Hadron Collider beauty experiment (LHCb), which specializes in investigating the differences between matter and anti-matter. It does this through the use of the beauty quark.

The production kinematics of the B^+ and B_c^+ mesons can differ as functions of transverse momentum and pseudo-rapidity. To understand the effects of the kinematic difference, a f_c/f_u correction is used. The fraction f_c/f_u is a ratio of the production fraction for the B_c^+ and the B^+ mesons. The results of this correction for the kinematic differences are then propagated through to determine its effect on efficiency and signal yield, which would impact the ability to determine the $B_c^+ \to \tau^+(\pi^+\pi^+\pi^-\overline{\nu_\tau})\nu_\tau$ branching fraction. This thesis considers **the feasibility to measure the $B_c^+ \to \tau^+\nu_\tau$ and $B^+ \to \tau^+\nu_\tau$ branching fractions using the LHCb detector**. A branching fraction measurement at LHCb would be important as the B_c^+ decay has not been experimentally observed before. However, measurements of this decay type are challenging. This is due to the neutrinos involved in the $B_c^+ \to \tau^+(\pi^+\pi^+\pi^-\overline{\nu_\tau})\nu_\tau$ decay, which cannot be detected; consequently, the B_c^+ decay vertex cannot be reconstructed. A B-tracking tool is used to infer the direction of the B_c^+ meson, which measures hits of the B_c^+ meson in the Vertex Locator sub-detector

rather than its decay products [2].

This research begins by diving into the theory surrounding the Standard Model and lepton flavour universality. After which, the LHCb and its technical and software components are discussed before leading into the theory behind B_c^+ production and branching fraction. This study of B_c^+ production leads to the derivation of a f_c/f_u correction, which is applied to the transverse momentum to correct for kinematic differences. Validation of the correction led to an unexpected issue involving negative transverse momentum, which was resolved by adapting the correction to a piece-wise function. The effect of the correction on the Vertex Locator (VELO) efficiency, sensitivity, and their implications are discussed with results from a maximum likelihood estimate providing information about signal yield. Finally, a discussion on the results is given, including areas for future improvement.

2 Theory

The concept of matter being made up of elementary particles has been around since at least the sixth century B.C.E. when Ancient Greek philosophers examined the philosophical idea of atomism [3]. In collisions of particles from progressively high-energy beams in the 1950s and 1960s, a bewildering diversity of particles were discovered. Informally, it was known as the "particle zoo". Physicists clarified the origin of the particle zoo in the decades after, leading to the establishment of the Standard Model in the 1970s.

Before looking at concepts such as production fraction, branching fraction, filtering efficiency and the possibility of new physics in lepton flavour universality, one must understand the Standard Model and the concepts that follow from it.

2.1 The Standard Model

The Standard Model (SM) is a theory that classifies all fundamental particles according to their properties and adds rules that govern which interactions can occur and at what rate. Tests have confirmed the SM with excellent precision, but physicists are still looking for observations demonstrating deviations from SM predictions and pointing toward new phenomena.

The Standard Model is written in the quantum mechanical framework of a relativistic quantum field theory (QFT), in which the particles are represented as fundamental fields. In the SM, there are two types of particles: bosons and fermions, which are then represented by bosonic and fermionic fields [4]. The classification between fermions and bosons is based on an intrinsic feature known as spin, which can be $(0, \frac{1}{2}, \text{or } 1)$ for elementary particles. Bosons are particles with integer spin $(0, 1)$, while fermions have half-integer spin $(\frac{1}{2})$. In interactions, fermions form the building blocks of quarks and leptons, while bosons are force carriers.

The charges carried by the fields add to their uniqueness where the colour is used to describe the charge associated with the strong interaction, which might be red, green, or blue. While quarks and leptons are elementary fermionic fields, only quarks possess a non-trivial colour charge; leptons do not. Quarks are then further divided into the up-type and down-type depending on their electric charge, which is related to the electromagnetic interaction. Up-type and down-type quarks have charges of $+\frac{2}{3}e$ and $-\frac{1}{3}e$ respectively. Leptons are broken down into electrically neutral neutrinos and charged leptons with charges of $1e$.

The elementary fermions are then divided into three families called the first, second, and third generations. Each generation contains an up-type quark, down-type quark, charged lepton, and a neutral neutrino. This results in a total of six quark flavours: up (u), down (d), strange (s), charm (c), bottom (b), and top (t) quarks, where the mass increases with each generation, and six leptons: electron (e), muon (μ), and tau (τ), as well as their accompanying neutrinos [5]. These are shown in Figure 2.1. Finally, each particle has an antiparticle with the same mass but an opposite quantum number.

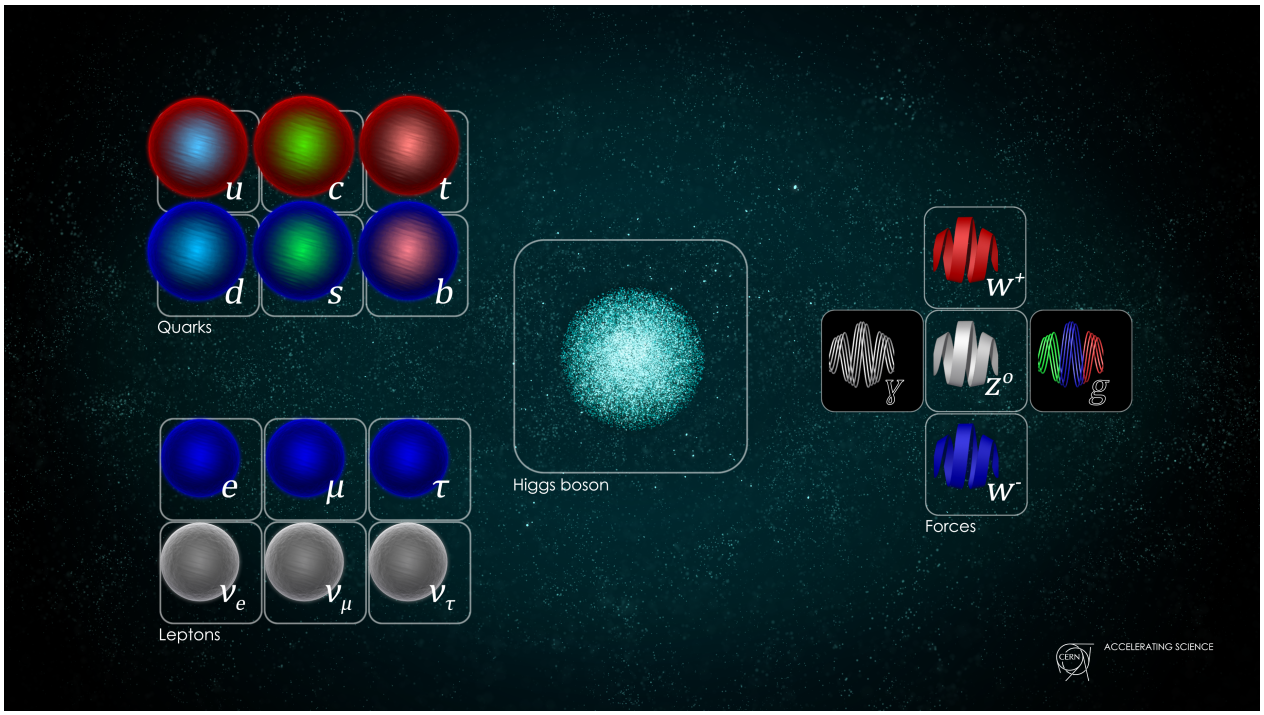

Figure 2.1: The particles within the SM occur in two types, quarks and leptons. The two groups each have six particles which are grouped in three generations. The SM also consists of the five force carriers and the special Higgs boson. Figure from [6].

Hadrons are particles composed of multiple quarks, while protons (uud) and neutrons (udd) are examples of baryons composed of three quarks. The B_c^+ $(\bar{b}c)$ and the B^+ $(\bar{b}u)$ contain a quark and an anti-quark and are called mesons.

All fermions interact through the weak force, which is mediated by $W^{\pm}$ and Z^0 bosons. There are two $W^{\pm}$ bosons, the W^+ and its antiparticle, the W^- while Z^0 bosons are their own antiparticle. The $W^{\pm}$ and Z^0 bosons are called gauge bosons as they act as the force carriers for elementary fermions. The fundamental fields associated with gauge bosons are called gauge fields, and gauge bosons are the excitations of those fields. Other bosons are photons (γ) and gluons (g), which carry the electromagnetic and strong

interaction, all of which have a spin of 1. The $W^{\pm}$ and Z^0 bosons are massive, while the other force carriers are massless. To explain the heavy masses of the $W^{\pm}$ and Z^0 bosons and generate the masses of the SM particles, one considers spontaneous symmetry breaking through the means of the Higgs field, which was first proposed by Brout and Englert [7] and Higgs [8].

It is essential to consider the concepts that the SM lacks, such as the particles that make up dark matter, the cosmological observation of the dominance of matter over antimatter, the universe's apparent dark matter composition, gravitons, and an explanation for the structure of matter [9].

2.2 Lepton Flavour Universality

The fact that the different leptons: electron (e), muon (μ), and tau (τ), have the same interaction strengths is a distinguishing property of the Standard Model. This is referred to as lepton flavour universality (LFU). The Higgs field is the only exception because the strength of the lepton–Higgs interaction causes the different lepton masses $m_\tau > m_\mu > m_e$.

On the other hand, lepton flavour universality is an unintentional symmetry of the SM, not a result of any of the theory's axioms. The SM's fundamental symmetries are used to explain the suppression of $b \to c l \nu$ transitions. Extensions to the Standard Model that address many of the model's shortcomings predict new virtual particles that could contribute to $b \to c l \nu$ transitions and have non-universal interactions, resulting in branching fractions of $B_c^+ \to \tau^+ (\pi^+ \pi^+ \pi^- \overline{\nu_\tau}) \nu_\tau$ decays with different leptons that differ from the SM predictions [9]. This opens the door to a violation of lepton flavour universality, which would be a clear sign of physics that goes beyond the Standard Model.

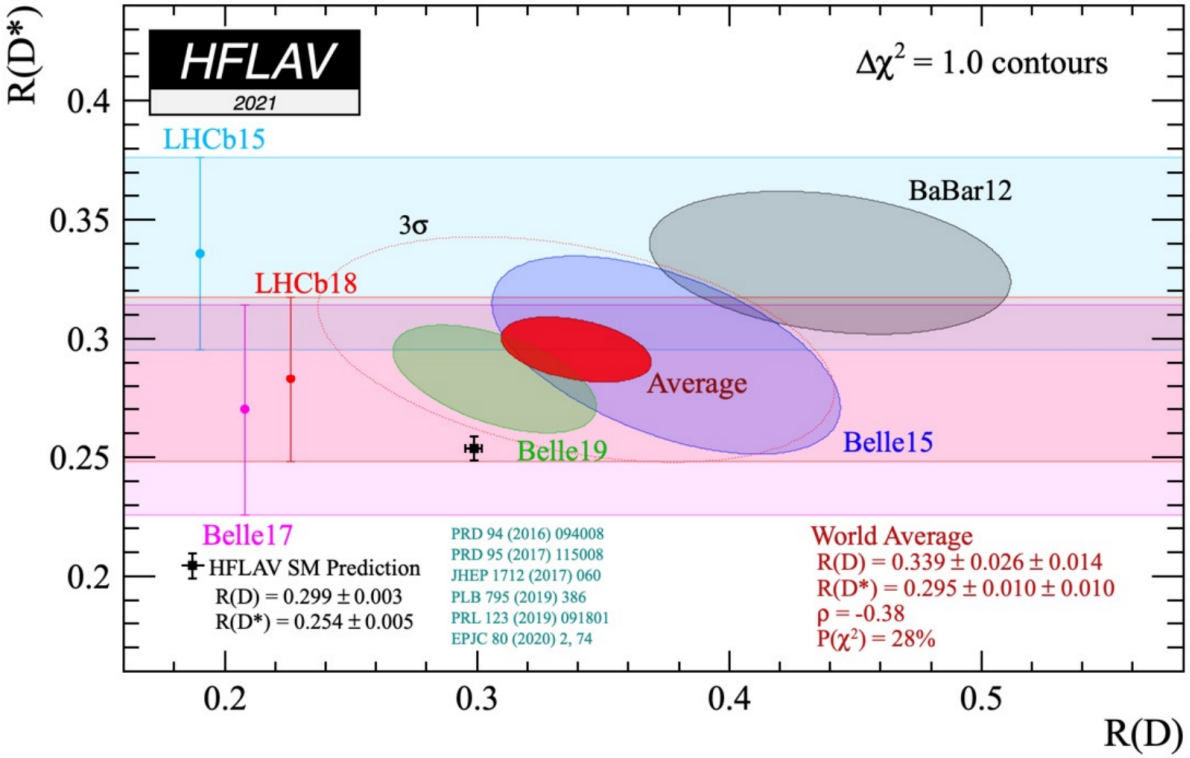

Figure 2.2: The Heavy Flavour Average Group average measurements of $R(D)$ and $R(D*)$. The red ellipse shows the combined average, while the data point shows the Standard Model prediction. Thus demonstrating a 3.1σ discrepancy. The branching ratios are defined as $R(D) = \mathcal{B}(B^+ \to \overline{D}^0 \tau^+ \nu_\tau)/\mathcal{B}(B^+ \to \overline{D}^0 l^+ \nu_\tau)$ and $R(D^*) = \mathcal{B}(B^+ \to \overline{D}^{*0} \tau^+ \nu_\tau)/\mathcal{B}(B^+ \to \overline{D}^{*0} l^+ \nu_\tau)$. Figure from [10].

The branching ratios of decays that differ only in lepton flavour are often compared to see if lepton flavour universality exists. Because all lepton flavours have the same coupling constant, lepton flavour universality determines these ratios precisely. Tension has evolved in $b \to s l^+ l^-$ and $b \to c l \nu_l$ transitions over the last decade or two, where (b), (s), and (c) are single quarks with the spectator quark omitted. Specifically, the $b \to c l \nu_l$ interaction has been previously measured in neutral and charged B-meson decays by B-factories Belle and Babar, and by LHCb, and the results from these experiments collectively show a deviation at the level of 3σ from Standard Model predictions, as seen in Figure 2.2 [11].

2.3 $B_c^+ \to \tau^+ \nu_\tau$

At the Large Hadron Collider (LHC), the large production cross-section of $b\bar{b}$ occurring in proton-proton collisions allows the LHCb experiment to collect large data sets used to perform high-precision measurements.

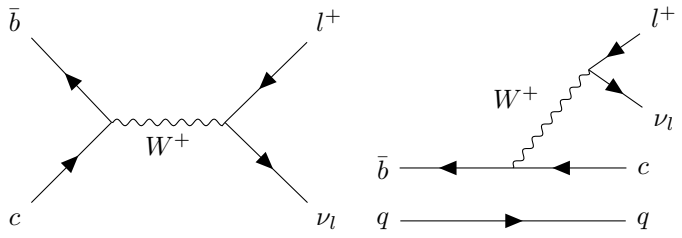

Figure 2.3: Feynman diagrams of $bc \to l^+ \nu_l$ (left) and $b \to c\, l^+ \nu_l$ (right) transitions, with the spectator quark $q \in \{u, d, c\}$.

To probe lepton flavour universality, tests often compare the branching fractions of decays which only differ regarding their lepton flavours. One such transition is $b \to c l^+ \nu_l$ which is identical to $bc \to l^+ \nu_l$ on the quark level. The transition $bc \to l^+ \nu_l$ describes that of the B_c^+ meson as seen in Figure 2.3. Thus, the leptonic pseudo-scalar meson decay $B_c^+ \to \tau^+ \nu_\tau$ is an experimentally and theoretically clean probe since the strong interaction only affects the B_c^+ state.

The LHCb collaboration previously used data with a corresponding integrated luminosity of $3.0\,\text{fb}^{-1}$ at center-of-mass energies of 7 and 8 TeV to report on the ratio of the branching fraction ($\mathcal{R}$) as seen in Equation (2.1) [12].

$$\mathcal{R}(J/\psi) = \frac{\mathcal{B}(B_c^+ \to J/\psi \tau^+ \nu_\tau)}{\mathcal{B}(B_c^+ \to J/\psi \mu^+ \nu_\mu)} \tag{2.1}$$

The LHCb collaboration found that the ratio of the branching fractions was measured to be within a 2σ deviation of those predicted by the Standard Model, as seen in Figure 2.2; however, for a new discovery to be considered, there must be at least a deviation of 5σ [12].

In the final state of B-meson decays with leptons, there exist possibilities for contributions toward new physics. This possibility is not present in processes using light leptons. This is because a new particle might couple at a 100% level to $b \to c\tau\nu$ and only at a 5% level to $b \to c\mu\nu$. Thus a measurement on the $B_c^+ \to \tau^+ (\pi^+\pi^+\pi^-\overline{\nu_\tau})\nu_\tau$ branching fraction could potentially lead to new observations on lepton flavour universality.

3
The Large Hadron Collider

The Large Hadron Collider beauty (LHCb) experiment is one of eight detectors at the Large Hadron Collider (LHC) at the Conseil Européen pour la Recherche Nucléaire (CERN). The experiments at CERN investigate a myriad of topics, from cosmic rays to supersymmetry.

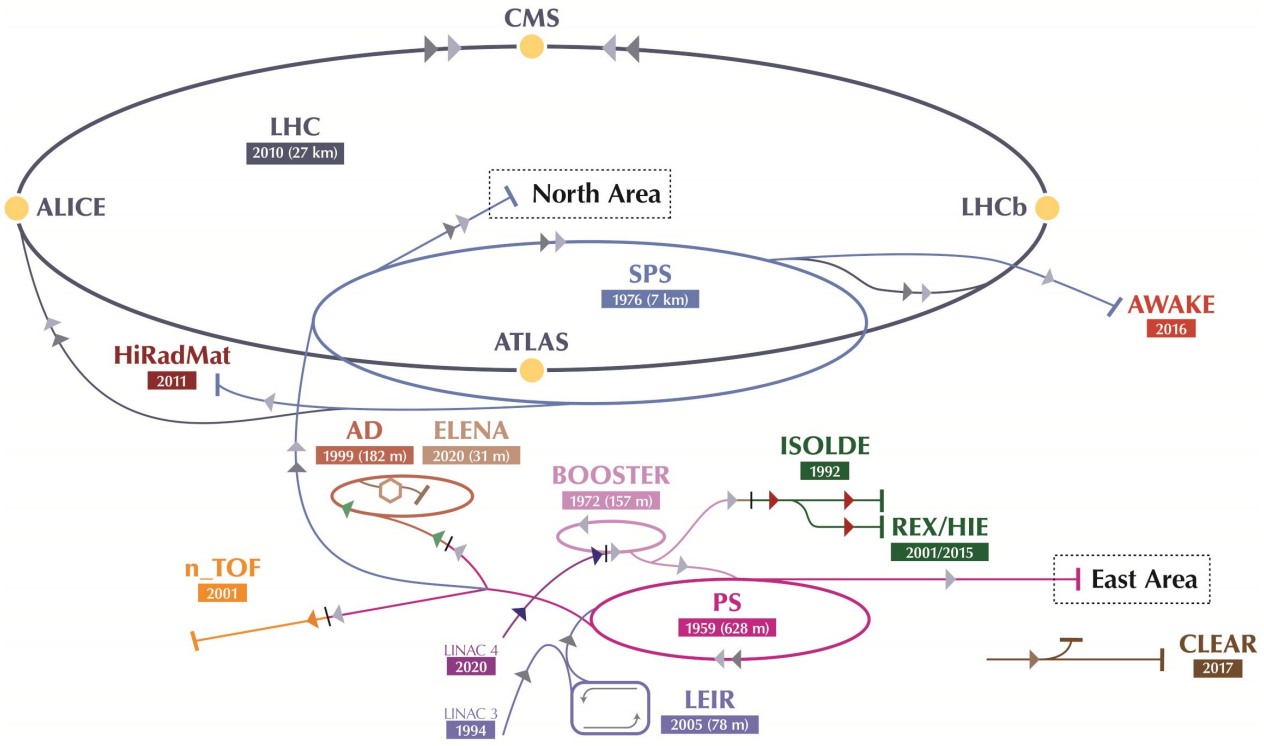

Figure 3.1: The CERN accelerator complex depicting the location of the LHCb interaction point. Figure from [13].

Four of these experiments, ATLAS, CMS, ALICE, and LHCb, observe the phenomenon of proton-proton (pp) collisions as seen in Figure 3.1. Two experiments, TOTEM and LHCf, concentrate on forward particles. The magnetic monopole is a hypothetical particle being looked for by MoEDAL-MAPP using detectors close to LHCb. Moreover, FASER, the newest LHC experiment, is located 480 meters from the ATLAS collision point to look for light new particles and analyse neutrinos.

The LHCb detector examines the beauty quark to understand the subtle variations between matter and antimatter. Rather than using an enclosed detector to encircle the collision point, the LHCb experiment uses a series of sub-detectors to detect predominantly forward particles – those propelled forward in one direction by the collision [13]. Research in this area could potentially explain the Universe's matter-antimatter asymmetry.

3.1 LHCb Detector

The LHCb is a single-arm forward spectrometer with a coordinate system that is right-handed Cartesian (x, y, z); the z-axis is defined as being parallel to the beam axis. A traditional cylindrical coordinate system utilising the same z-axis can also use a system with the polar angle (θ) and the transverse azimuthal angle (ϕ), which are relative to the z and x-axes respectively. The LHCb alternates the traditional cylindrical coordinate system so that the polar angle (θ) is replaced with the pseudo-rapidity (η). Thus the cylindrical coordinate system is defined through (z, η, ϕ).

Pseudo-rapidity is mathematically defined by Equation 3.1 where θ is the angle between the particle's three-momentum and the positive direction of the beam axis.

$$\eta \equiv -\ln\left[\tan\left(\frac{\theta}{2}\right)\right] \tag{3.1}$$

The single-arm forward spectrometer design has a pseudo-rapidity range of $2 < \eta < 5$ since many b-hadrons are produced at small polar angles [14]. The pseudo-rapidity range corresponds with a polar angle range of $0.77° < \theta < 15.4°$.

3.1.1 LHCb Run 3 Upgrades

In December 2018, the LHC shut down for three years of maintenance and upgrades, known as the Long Shutdown 2 (LS2). LS2 allowed for upgrades to the LHC, the accelerator, ALICE, ATLAS, CMS, and the LHCb. The LHC has previously done two runs named run one and run two, which ran from 2010-2013 and 2015-2018, respectively.

During LS2, six significant changes were made to the LHCb. These include upgrades to the VELO, the two ring-imaging Cherenkov (RICH) detectors, the upstream tracker (UT), the replacement of the three tracking stations after the magnet with a new station using scintillating fibres (SciFi), and new front-end electronics as seen in Figure 3.2.

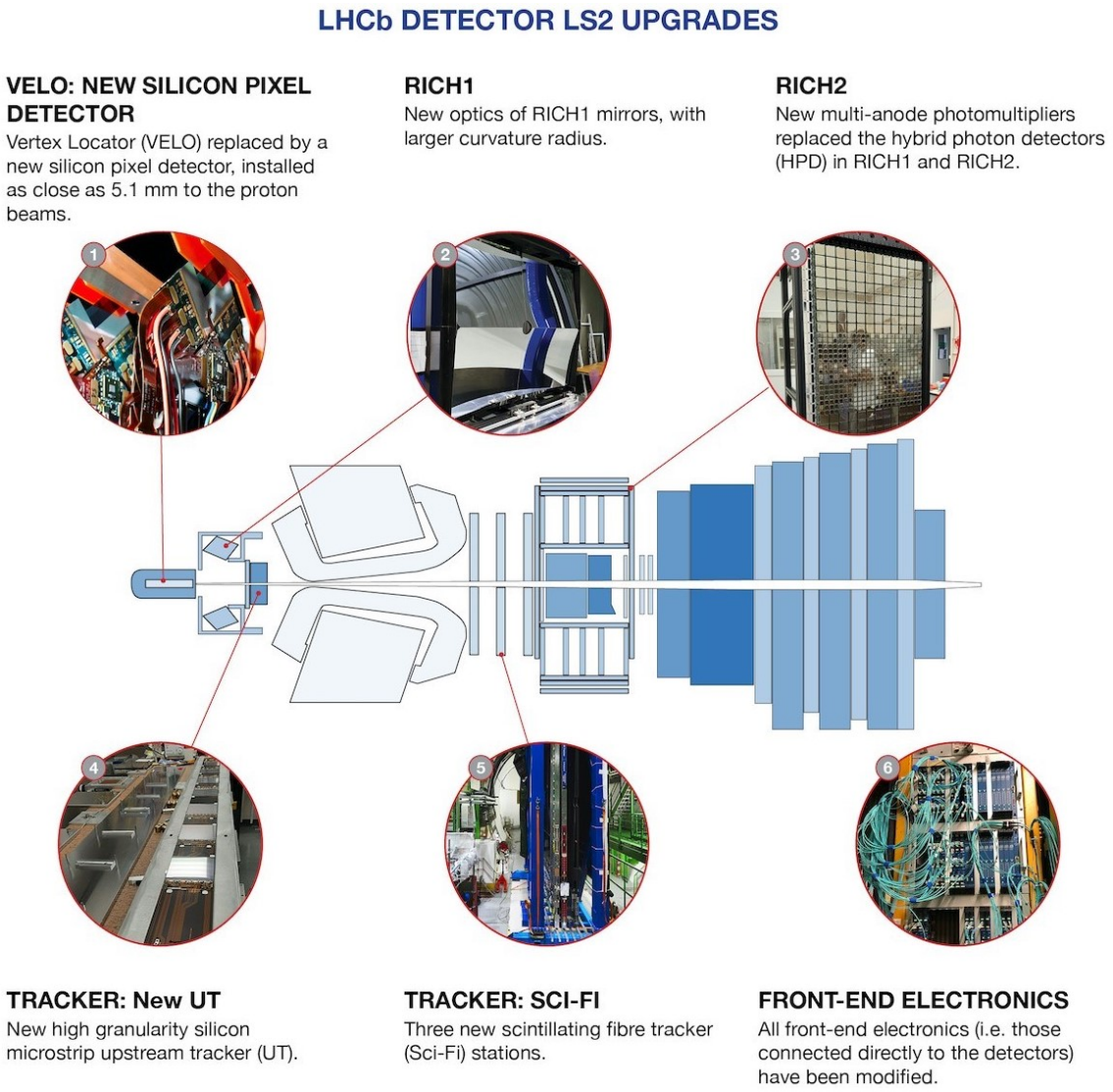

Figure 3.2: The LHCb upgrades during the Long Shutdown 2 showing the locations of the upgrades to the VELO, RICH 1, RICH2, the new UT tracker, the new SciFi tracker, and the upgrades to the front-end electronics. Figure from [15].

The vertex locator (VELO) is a sub-detector that measures the distance between the collision point and the decay point of b-hadrons [15]. Pixel-tracking layers are used in the new VELO, improving hit resolution and making track reconstruction easier. It is also closer to the beam axis, at 5.1 mm rather than 8.4 mm. For this reason, the VELOPIX chip was developed, capable of gathering signal hits from 256×256 pixels and delivering data at a staggering pace of up to 20 Gb/s.

The particle identification system uses the Ring Imaging Cherenkov (RICH) and muon detectors to determine the identity of the charged particles. The RICH detectors can determine the identity of the charged particles by measuring the velocity, which is then combined with the momentum to estimate the mass. Muons produced at LHCb are minimally interacting particles; thus, they transverse the calorimeter system; hence, the muon stations (M1-M5) are used to reconstruct the muon tracks.

RICH1 and RICH2 enable good particle identification over a wide momentum range [15]. Both have been upgraded to handle the more difficult data-gathering conditions of LHC Run 3. The RICH1 detector's optical system has been improved such that its optics have been altered to distribute the Cherenkov rings over a broader surface to lower the number of photons in the hottest zone. The system for detecting photons has been redesigned such that for detecting single photons, two types of 64-channel multi-anode photomultiplier tubes with outstanding spatial resolution and low background noise were chosen.

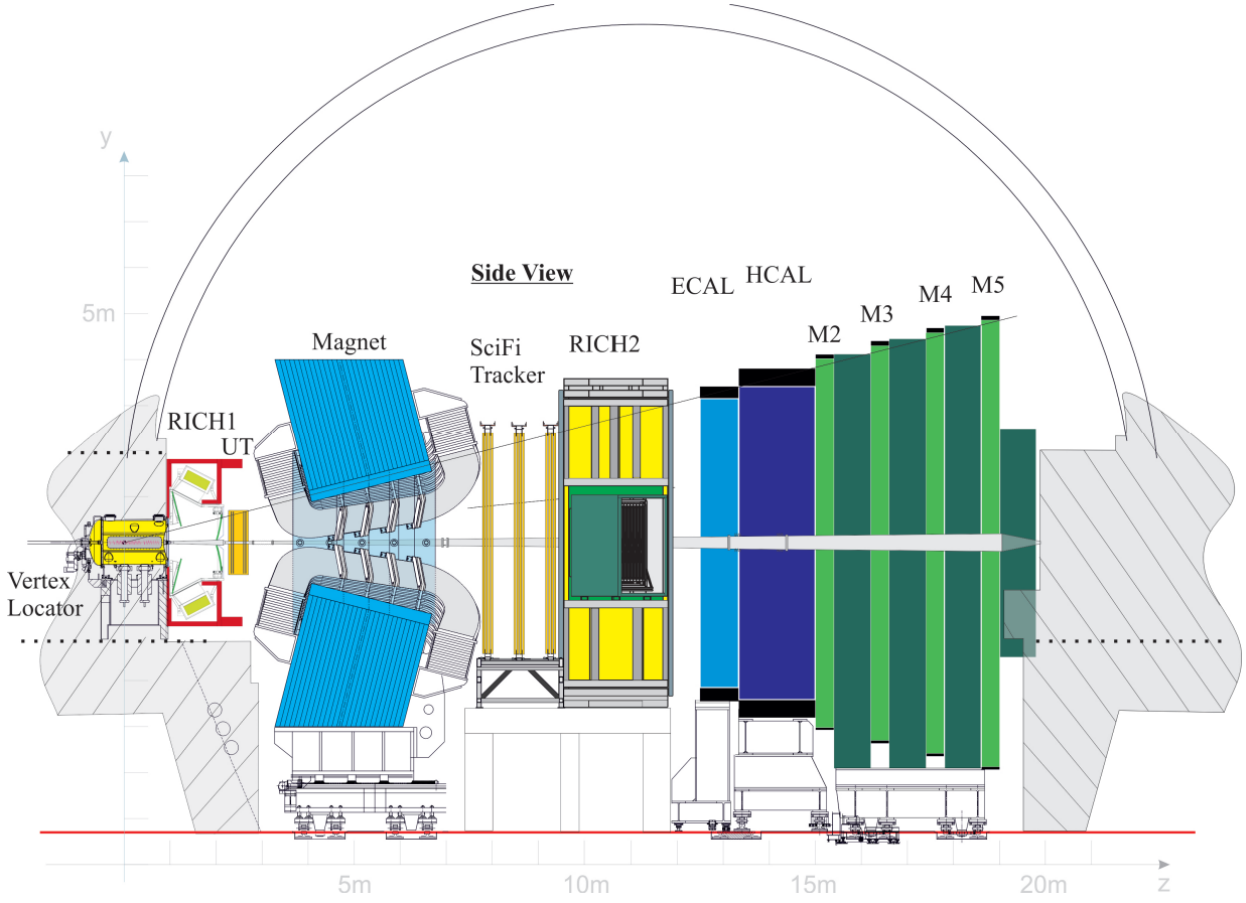

Figure 3.3: Depiction of the upgrade 3 LHCb detector and its components. Major components include the Vertex Locator (VELO), the Ring Imaging Cherenkov detectors (RICH1 and RICH2), the Upstream Tracker (UT), the SciFi Tracker, the Calorimeters (ECAL, HCAL), and Muon Stations (M1, M2, M3, M4, M5). Significant changes to the Run 3 detector include the Upstream Tracker (UT) and the Scintillating Fibre Tracker (SciFi). Figure from [16].

Originally, the main tracking system relied on four tracking stations to reconstruct charged particle paths: one between RICH1 and the LHCb dipole magnet and three between the magnet and RICH2 [15]. In place of the station before the magnet, a new upstream tracker (UT) has been fitted with silicon-microstrip sensors. After the magnet, the three tracking stations were replaced with a new type of station based on scintillating fibres (SciFi), which were read out at one end by silicon photomultiplier (SiPM) arrays. The detector is constructed of scintillating fibres, which are optical fibres that emit light when a particle interacts with them, as the name suggests. The sub-scintillating detector's fibres have a diameter of 0.25 mm and a length of about 2.5 m. The UT and SciFi tracker locations can be seen in Figure 3.3.

The calorimeter system uses calorimeters to measure the energy of electrons, photons, and hadrons. Particles that interact electromagnetically utilise the Electronic Calorimeter (ECAL). Finally, the Hadronic Calorimeter (HCAL) measures hadron energy.

Every 25 ns, the beams in the LHC cross in a detector, equating to a frequency of 40 MHz [15]. In past years, LHCb filtered this event rate down to 1 MHz, selecting the most intriguing events with rapid electronics. These occurrences were then further processed and filtered. However, starting in 2022 with Run 3, the entire detector will read at the full rate of 40 MHz, allowing the program to identify events more precisely and flexibly. As a result, the electronics of nearly all of the sub-detectors have been upgraded, and the LHCb event selection system's (the trigger) computational capability will be increased. The Front-End electronics will use the Gigabit Transceiver (GBT), a radiation-resistant chipset, for reading, slow control, monitoring, and synchronisation.

3.2 LHCb Software

A typical difficulty in particle decay analysis is understanding the kinematic features of a signal decay and the potential backgrounds that are potentially contributed to other particle decays that are inadequately reconstructed in the detector. The potential backgrounds mentioned could come from various places; however, two examples include decays to final states containing a subset of the particles in the signal decay and decays to final states containing identical particles as the signal decay with other particles that the detector is not asked to reconstruct [17].

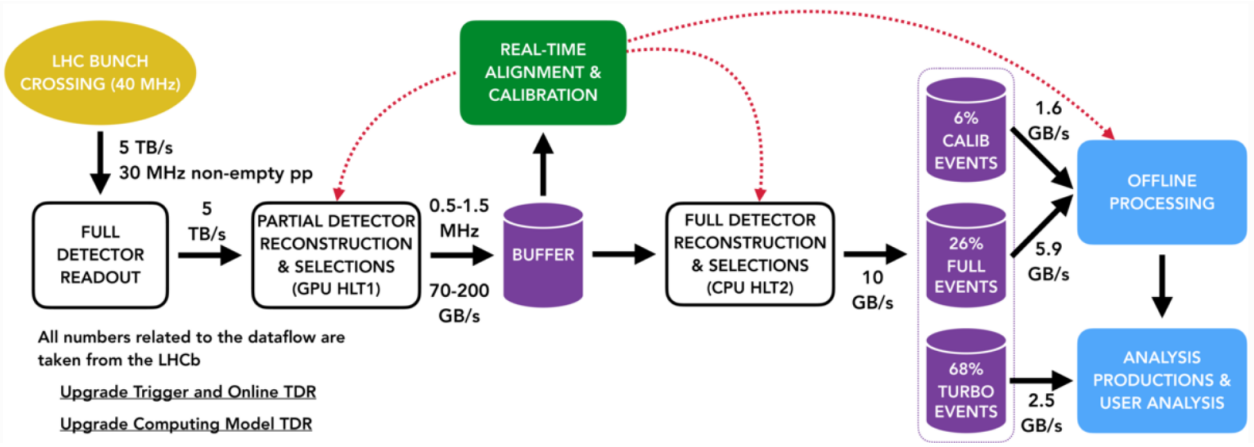

Figure 3.4: The LHCb software trigger system for the Run 3 upgrade. The upgrade included the removal of the hardware trigger which was exchanged with this fully software based trigger. This removes a limitation that the hardware trigger imposed on luminosity. Figure from [18].

To investigate potential background sources, huge samples of decays can be generated and run through the entire detector simulation and reconstruction software chain. Figure 3.4 shows the LHCb Run 3 trigger system, including the steps between the full detector readout to the analysis productions and user analysis. The shape of the background can then be investigated by selecting these events as if they are signal. This process is lengthy due to the time it takes to generate and reconstruct data, including a full simulation of the detector components and the significant amount of storage space needed to store all the data. RapidSim is an application which potentially solves this problem.

3.3 Cross Section, Luminosity, & Rate

Before considering production and branching fractions and their possible impacts on sensitivity, it is vital to understand the concepts of cross-section and luminosity within a collider.

Within a collider, the cross-section (σ) is a measurement of the probability that an event occurs, two particles colliding, which is measured in barns ($1\text{b} = 10^{-24}\text{cm}^2$). Particles with larger cross-sections are by definition expected to be observed more frequently.

The number of events that occur per second, for some decay, can be calculated using Equation (3.2) which shows a dependence on the luminosity (L).

$$N_{\text{events/sec}} = L\sigma_{\text{event}} \tag{3.2}$$

The luminosity (L) is a measurement of the number of collisions that can be produced in a detector. The larger the luminosity value, the more collisions occur leading back to Equation (3.2). Luminosity can be integrated such that one obtains the integrated luminosity (L_{int}), defined by Equation (3.3), which is a measurement of the collected data size. The integrated luminosity is a crucial value used when investigating the performance of an accelerator.

$$L_{\text{int}} = \int L dt \tag{3.3}$$

Equation (3.2) describes how many events one expects to measure, however, this implies a perfect detector. Therefore one must consider the other contributing factors. This leads to the rate equation, Equation (3.4). The rate equation also uses the variables for branching fraction (Br), acceptance (Acc), and efficiency (Eff).

$$N = L\sigma \cdot \text{Br} \cdot \text{Acc} \cdot \text{Eff} \tag{3.4}$$

A particle can decay through many different channels, and while some of these decays can be measured by detectors, others cannot. The branching fraction (Br) is the fraction of particles that decay through a specific path. This leads to the acceptance (Acc) or fraction of decays in which all the final state particles are in the region the detector can measure. Finally, the efficiency (Eff) is the fraction of events that were measured after detector reconstruction and selection. This leads to a study of the $B_c^+ \to \tau^+(\pi^+\pi^+\pi^-\overline{\nu_\tau})\nu_\tau$ filtering efficiency in Chapter 7.

4

B_c^+ Production

The production kinematics of the B^+ and B_c^+ mesons can differ as functions of transverse momentum and pseudo-rapidity. Therefore, the production fraction needs to be measured as a function of those variables.

The B_c^+ mesons are the only states in the Standard Model formed by two heavy quarks of different flavours; in this case, the $\bar{b}$ and c quarks. The production of the B_c^+ meson within the context of a (pp)-collision requires a simultaneous production of $b\bar{b}$ and $c\bar{c}$ pairs. This causes it to be rarer than that of other b-mesons.

For B_c^+ mesons, created through (pp)-collisions in the LHC, the dominant production mechanism is gluon-gluon fusion (ggF) as seen in Equation (4.1). The representative Feynmann diagram is shown in Figure 4.1. Gluon-gluon fusion occurs when two gluons interact together into order to create a particle.

$$gg \rightarrow B_c + b + \bar{c} \tag{4.1}$$

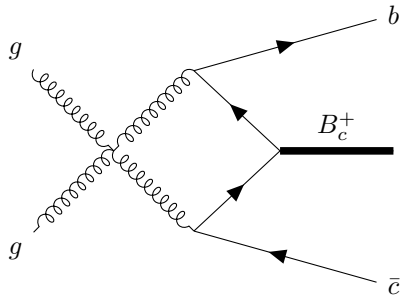

Figure 4.1: Feynman Diagram for the gluon gluon fusion $gg \rightarrow B_c + b + \bar{c}$.

4.1 B_c^- Production Fraction

The B_c^- production can be described by a production fraction that can be denoted through relative branching fractions as seen in Equation (4.2).

$$\frac{f_c}{f_u + f_d} = \frac{n_{\text{corr}}(B_c^- \to J/\psi\mu^-\overline{\nu})}{n_{\text{corr}}(B \to D^0 X\mu^-\overline{\nu}) + n_{\text{corr}}(B \to D^+ X\mu^-\overline{\nu})} \cdot \frac{\langle \mathcal{B}_{sl} \rangle}{\mathcal{B}(B_c^- \to J/\psi\mu^-\overline{\nu})} \tag{4.2}$$

The variables f_c, f_u, f_d respectively denote the production fractions of the respective decays for B_c, B_u, and B_d. The production fraction is the number of particles of that type generated during a (pp)-collision. The branching fraction is denoted by $\mathcal{B}$, of the corresponding decay rate, and $\mathcal{B}_{sl}$ denotes the average branching fraction of B^+ and B_d mesons. The variable n_{corr} denotes the efficiency corrected yield and thus $n_{\text{corr}}(B_c^- \to J/\psi\mu^-\overline{\nu})$ describes the efficiency corrected yield for that specific mode.

4.2 Production Fraction Correction for Transverse Momentum

The article *Measurement of the B_c^- meson production fraction and asymmetry in 7 and 13 TeV pp collisions* [19] considers the corrections to the transverse momentum for the B_c^- meson. Firstly, a correction factor (k), a ratio of the average p_T to $\text{p}_{\text{T, TRUE}}$ as a function of hadron and muons invariant mass, was found. Due to the missing neutrinos, the true transverse momentum in the production measurement is based on reconstructed transverse momentum. This correction is different for the two modes as each mode reconstructs a certain decay. Specific to the B_c^- decay, the average correction varied from 0.75 to unity for the B-meson over the range of 3 GeV to the B-mass and from 0.85 to unity for the B_c^- meson over the range of 4 GeV to the B_c^- mass. This correction factor (k) is required for the for the modes considered in Equation (4.2) to measure n_{corr} versus $\text{p}_{\text{T, TRUE}}$ correctly.

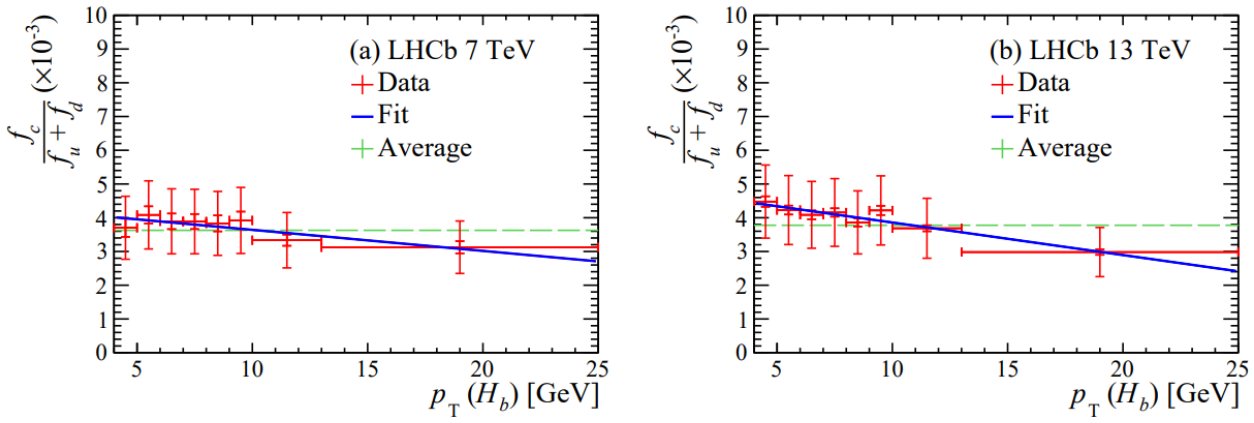

Figure 4.2: The ratio of the production fractions as a function of transverse momentum after a k-factor correction. The k-factor correction is the ratio of the average reconstructed to true transverse momentum as a function of the invariant mass. Image from [19].

Thus it was shown that the fraction $f_c/(f_u + f_d)$, which is a ratio of production fractions, has a dependence on transverse momentum with the dependence on the pseudo-rapidity being small. This dependence is shown in Equation (4.3).

$$\frac{f_c}{f_u + f_d}(p_T) = A[p_1 + p_2(p_T(H_b) - \langle p_T \rangle)] \tag{4.3}$$

The variables are the overall normalization $A = 1 \pm 0.24$ which includes the global systematic uncertainty, the average transverse momentum $\langle p_T \rangle = 7.2$ GeV, and the slopes p_1, and p_2. The values for the slopes p_1 and p_2 are given in the article *Measurement of the B_c^- meson production fraction and asymmetry in 7 and 13 TeV pp collisions* [19].

Energy	p_1	$p_2 \cdot 10^{-2}$ (GeV^{-1})
13 TeV	$4.13 \pm 0.05 \pm 0.04$	$-9.7 \pm 0.8 \pm 1.0$

Table 4.1: Results for p_1 and p_2 for an energy value of 13TeV. Results taken from *Measurement of the B_c^- meson production fraction and asymmetry in 7 and 13 TeV pp collisions* [19]

4.3 Production Fraction Correction Applied to the B_c^+

When measuring the $B_c^+ \to \tau^+(\pi^+\pi^+\pi^-\overline{\nu_\tau})\nu_\tau$ decay, it should be compared with a similar decay mode to the decay being studied. This is done to reduce systematic uncertainties and eliminate the effects of hadron creation; it is a usual practice to assess signal modes relative to a normalization decay. Regarding the B_c^+ , its counterpart is the B^+ . The normalization mode for the B^+ meson is $B^+ \to D^-(\pi^-\pi^-\pi^+)\pi^+\pi^+$ for the $B_c^+ \to \tau^+(\pi^+\pi^+\pi^-\overline{\nu_\tau})\nu_\tau$ analysis.

Due to their low mass, the number of up (u) and down (d) quarks produced at LHCb collisions are similar; therefore, $f_d \approx f_u$ holds. Thus, Equation 4.2 is transformed into Equation 4.4. This transformation between the B_c^- to B_c^+ mode is allowed through the implication of charge conjugation.

$$\frac{f_c}{2f_u} = \frac{n_{\text{cor}}(B_c^+ \to \tau^+\nu_\tau)}{n_{\text{cor}}(B^+ \to \tau^+\nu_\tau)} \cdot \frac{\mathcal{B}(B^+ \to \tau^+\nu_\tau)}{\mathcal{B}(B_c^+ \to \tau^+\nu_\tau)} \tag{4.4}$$

Thus the fraction $f_c/(f_u + f_d)$, which is a ratio of production fractions, is shown in Equation (4.5).

$$\frac{f_c}{f_u}(p_T) = 2A[p_1 + p_2(p_T(H_b) - \langle p_T \rangle)] \tag{4.5}$$

The number of fitted B_c^+ mesons can be seen as a combination of the number within the data-set multiplied by the efficiency as seen in Equation (4.6). The number of B_c^+ mesons in the data-set is determined by combining the luminosity, the cross-section of the (pp)-beam, the production, and the branching fraction as seen in Equation 4.6.

$$N_{\text{fit}}(B_c^+ \to \tau^+\nu_\tau) = N_{\text{data-set}}(B_c^+ \to \tau^+\nu_\tau) \cdot \epsilon_{\text{detector}}(B_c^+ \to \tau^+\nu_\tau) \tag{4.6}$$

At LHCb, this is measured as a ratio in comparison to the normalization mode of the B^+ meson as seen in Equation (4.7). During this research, the fraction $\epsilon_{B^+}/\epsilon_{B_c^+}$ and its effects on N_{fit} are primarily considered. This is discussed in depth in Chapter 5.

$$\frac{\mathcal{B}(B_c^+ \to \tau^+ \nu_\tau)}{\mathcal{B}(B^+ \to D^- \pi^+ \pi^+)} = \frac{N_{\text{fit}} B_c^+}{N_{\text{fit}} B^+} \cdot \frac{f_u}{f_c} \cdot \frac{\epsilon_{B^+}}{\epsilon_{B_c^+}} \tag{4.7}$$

5
Analysis Strategy

With the concepts of the Standard Model, lepton flavour universality, and the motivation behind studying the $B_c^+ \to \tau^+(\pi^+\pi^+\pi^-\overline{\nu_\tau})\nu_\tau$ decay theorised, one thus considers the analysis strategy for this research.

Before looking into production and branching fractions, data for the transverse and true transverse momentum must be simulated and analysed. This is done via RapidSim which is executed through the ROOT [20] software package as discussed in section 5.1. This leads to a discussion of the difference between unfiltered and filtered data and the transformation that morphs one into the other, as discussed in section 5.3.

After creating simulation data and understanding the difference between the two data types, one considers the B_c^+ meson and its production kinematics. Due to the simulatory nature, VELO hits are inferred. This leads to a strategy for analysing production and branching fractions through a correction applied to the B_c^+ transverse momentum values. This correction accounts for the kinematic differences between B^+ and B_c^+ mesons. Thus one considers the analysis that takes place on the kinematics, including an investigation of the differences between transverse and true transverse momentum as discussed in section 5.4.

The f_c/f_u correction for the kinematic differences is then applied to the VELO efficiency to determine its effect on efficiency, signal yield, uncertainty, and sensitivity as discussed in section 5.5. This is done through a maximum likelihood fit which uses variables from a multivariate analysis.

5.1 Data Generation & Analysis Through RapidSim & Root

RapidSim allows large samples of potential signal and background decays, including momentum spectra, invariant mass resolutions, and efficiency shapes, to be quickly generated [17]. These data sets are close approximations to what would be obtained if a full detector simulation was run. RapidSim allows the user

to create a single decay chain with unlimited sub-decays. RapidSim can thus be thought of as a Monte Carlo generator though it boasts faster generation; because it does not simulate the underlying event (the (pp)-collision), the detector response or reconstruction, only the decaying particle (the B meson).

The ROOT software package executes the fast generation of RapidSim. ROOT makes it possible to conduct statistically sound scientific investigations and visualise vast amounts of data. With its substructures, branches and leaves, the data container tree is a crucial aspect of ROOT. A tree can be considered a sliding window into the raw data in a file, and advancing the index in the tree allows retrieval of data from the next entry in the file. This eliminates the memory allocation issues with object creation, allowing the tree to function as a lightweight container while handling buffering discreetly [21]. Because data from the Large Hadron Colliders experiments is projected to be many petabytes per year, ROOT is built for high computational efficiency. It is used daily by thousands of physicists to analyse data and perform simulations [21].

5.2 Charged Tracking & B-Tracking Tool

The reconstruction process begins in the VELO, where straight sequences of hits in the modules are detected [2]. A (pp)-collision is expected to have occurred at one or more of the primary vertices, which is then reconstructed by using line segments that lead to that location as seen in Figure 5.1. To investigate additional hits which occurred in the primary tracking stations before and after the magnet, the line segments are extended downstream; this is known as forward tracking. The (pseudo)-stable particles are detected using data from the detector's other components as well. These final state particles are used to infer the existence of short-lived particles such as b and c mesons.

If a B_c^+ decay is detected using the final state particles, the decay can be linked to VELO hits if the meson has not already prematurely decayed. The goal of B-Tracking is to infer the direction of charged B-meson decays when it leaves one or more VELO hits; neutral particles do not cause VELO hits. It should be noted, that in RapidSim no hits occur in the VELO due to its nature as a simulation; rather hits are inferred to have been on the PV-SV line through the VELO.

5.3 Unfiltered Versus Filtered Data

As previously discussed, RapidSim allows large quantities of data to be generated through the second decay into pions during $B_c^+ \to \tau^+(\pi^+\pi^+\pi^-\overline{\nu_\tau})\nu_\tau$. These data sets are considered unfiltered data. To morph the unfiltered data into filtered data, hits in the VELO are considered. The critical difference between the unfiltered and filtered data is the requirement of a hit in the VELO occurring.

A B-meson has a flight distance that corresponds to the location of the secondary vertex (SV) minus the primary vertex (PV), as seen in Equation (5.1).

$$\overrightarrow{FD} = \overrightarrow{SV} - \overrightarrow{PV} \tag{5.1}$$

The z-axis was previously defined as being parallel to the beam axis. Thus consider z_{active} as the distance that the particle travels inside the VELO along the z-axis, which is defined by Equation (5.2). The variable r_{in} represents the inner radius of the VELO, and θ is the angle between the flight direction of the B-meson

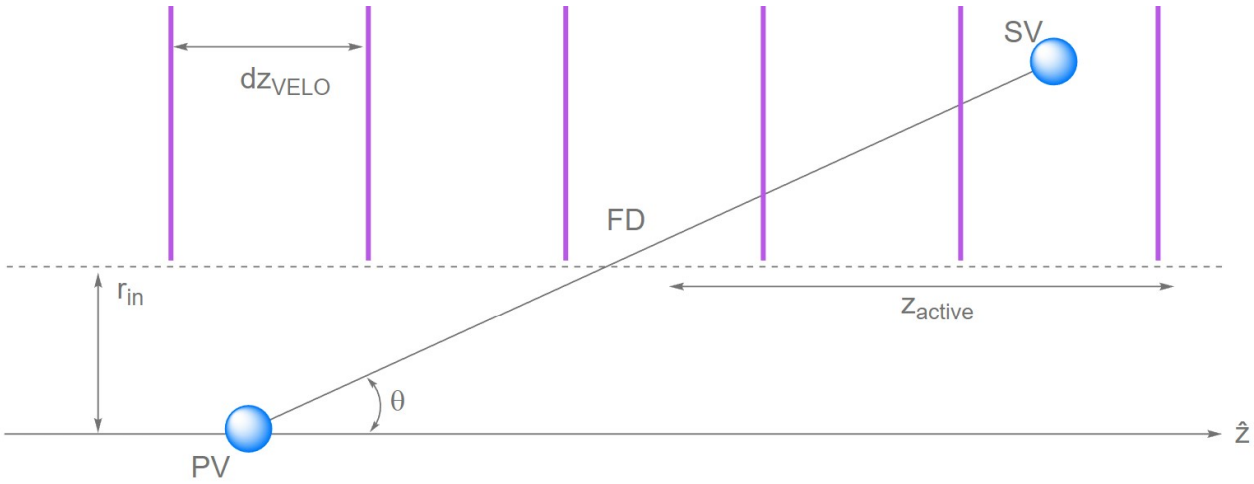

Figure 5.1: The purple lines represent the VELO modules and the variables used to estimate the number of VELO hits. This mimics the B-Tracking Tool.

and the z-axis.

$$z_{\text{active}} = (|\overrightarrow{FD}| - r_{\text{in}}) \cot\theta \tag{5.2}$$

The number of hits by a single B-meson is calculated through Equation (5.3) where ϵ is a random number and accounts for the fact that the PV is uniformly distributed between two VELO modules, assuming that the B_c^+ primary vertex distribution is flat in the VELO region. The events with $N_{\text{hit}} \geq 1$ are selected.

$$N_{\text{hit}} = \left\lfloor \frac{z_{\text{active}}}{dz_{\text{VELO}}} + \epsilon \right\rfloor \tag{5.3}$$

The number of events (or entries) in the filtered data thus becomes the number of events corresponding to a VELO hit.

5.4 B_c^+ Production & Kinematics Including Validation Ratios

The transverse and true transverse momentum for the B^+ and B_c^+ are investigated for both the unfiltered and filtered data. The requirement for the hit in the VELO is a critical distinguishing difference; therefore, a focus is put on understanding the requirement's effects. After analysing the differences between the two data types, the f_c/f_u weighted correction, as seen in Equation (4.5), is applied to both data sets. The combination of the requirement on the filtering and the effect of this weighted correction is studied to understand how the filtering and the correction affect the B_c^+ kinematics compared to that of the B^+ kinematics.

To validate the results, the ratio of B_c^+ /B^+ was graphically represented for the unfiltered and filtered data. An issue occurred with the f_c/f_u correction causing negative transverse momentum values to occur above a transverse momentum value of approximately 50 GeV. To resolve this issue, a piece-wise function approach was applied to the f_c/f_u correction. This is discussed in detail in section 6.3.1.

5.5 Filtering Effect on VELO Efficiency

The investigation of the B_c^+ kinematics aims to find information on how the filtering process affects the data. To build on this idea, the research thus considers how the f_c/f_u correction affects filtering efficiency.

To determine filtering efficiency, the average number of filtered weights is divided by the average number of unfiltered weights, thus getting a representative ratio of the filtering effect. This value is then multiplied by the existing VELO efficiency to determine the f_c/f_u corrected VELO efficiency.

To estimate the B_c^+ yield in the sensitivity study, a maximum likelihood fit is used to extract the signal yield from a dataset which contains the B_c^+ signal, the B^+ signal, and the signal of the most dangerous background, the $B^+ \to D^0\pi^+\pi^+\pi^-$. The maximum likelihood fit uses a multivariate analysis's corrected mass and variables. This allows for the signal yield and uncertainties for the original VELO efficiency and the f_c/f_u corrected VELO efficiency to be compared, and the effects on sensitivity are discussed.

6

Study of B_c^+ Meson Kinematics

In this chapter, the B_c^+ kinematics are studied by investigating the transverse and true transverse momentum for both the unfiltered and filtered data. Transverse momentum (p_T) is the component of momentum which is transverse, or perpendicular, to the beam line. This definition of momentum is used as the transverse momentum always results from the event at the vertex, while momentum in the z-direction could be remnants from the beam itself. After understanding these differences, the production fraction correction of the transverse momentum or weighting from Equation (4.5) is applied to the B^+ and B_c^+ kinematics.

6.1 Transverse & True Transverse Momentum

Before investigating the dependence of transverse momentum on production fraction, the difference between transverse and true transverse momentum is discussed.

The true transverse momentum ($p_{T,\,TRUE}$) is the true transverse momentum generated based on "Fixed Order + Next-to-Leading Log" (FONLL) [22] of the transverse momentum histogram. In contrast, the transverse momentum (p_T) is the reconstructed momentum of the three pions in the decay, which emulates the resolution on the momentum. When the transverse momentum of a heavy quark is significantly larger than its mass, FONLL quantum chromodynamics is matched with all-order resummation to next-to-leading log precision. It lets one construct predictions for one-particle inclusive distributions of a heavy quark (or heavy hadron) while the other particles' degrees of freedom are integrated over.

During the decay of B_c^+ to three pions ($B_c^+ \to \tau^+(\pi^+\pi^+\pi^-\overline{\nu_\tau})\nu_\tau$), the first decay into $\tau^+\nu_\tau$ is untraceable as well as the anti-neutrino $\overline{\nu_\tau}$ in the second decay. The three pion data, excluding the anti-neutrino, is smeared to create the reconstructed transverse momentum (p_T). This smearing is done using the data from the second decay into three pions and an anti-neutrino. To better understand these differences,

graphs depicting p_T and $p_{T,\,TRUE}$ for both the B^+ and B_c^+ decays were plotted.

Figure 6.1 demonstrates the difference between the transverse and true transverse momentum for the unfiltered data. The p_T values for the B_c^+ and B^+ decays show a lower transverse momentum peak (approximately 1.75 GeV) than the $p_{T,\,TRUE}$ values for the same decays (approximately 3 GeV). The average transverse momentum for the B^+ decay is 2.80 GeV, with its true momentum counterpart having an average value of 5.32 GeV. Conversely, the values for the B_c^+ decay are 2.96 and 5.32 GeV for the p_T and $p_{T,\,TRUE}$ values respectively. Thus demonstrating a difference between p_T and $p_{T,\,TRUE}$ of approximately 2.4 GeV.

Hence, it can be concluded that the $p_{T,\,TRUE}$ is higher on average than the corresponding p_T . This is due to the difference in definition between the two reconstructions of the transverse momentum. The p_T is the smeared pions that follow from the decay $B_c^+ \to \tau^+(\pi^+\pi^+\pi^-\overline{\nu_\tau})\nu_\tau$; however, it does not reconstruct the neutrinos. The $p_{T,\,TRUE}$ using FONLL knows which B_c^+ momentum was used, which leads to the difference between the transverse momentum peaks.

The average p_T for the B^+ and B_c^+ decays are 2.80 and 2.96 GeV respectively showing a difference of 0.16 GeV. Conversely, for the average $p_{T,\,TRUE}$ the values are 5.32 and 5.32 GeV, respectively. Hence there is little to no difference between the B^+ , and B_c^+ decays for the average transverse and true transverse momentum for the unfiltered data.

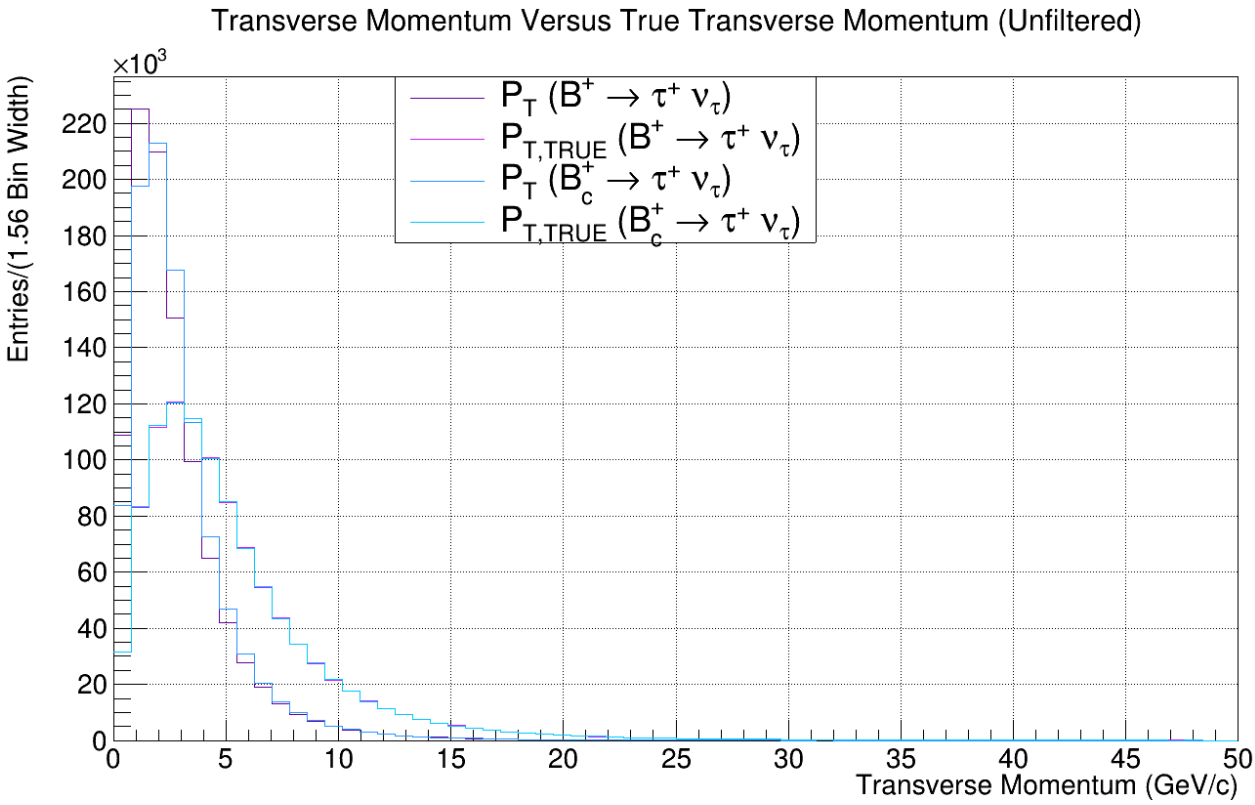

Figure 6.1: The values for the transverse momentum for the B^+ and B_c^+ decays using unfiltered data.

The graph in Figure 6.1 was then recreated for the filtered data, and is presented in Figure 6.2. Visually the graph shows similar shape trends compared to the unfiltered data; however, the peaks of the B^+ curves and the corresponding transverse momentum values differ greatly. The B_c^+ decays are eclipsed by the size of the B^+ decays after filtering and thus were sectioned into a new plot as seen in Figure 6.3.

For the B^+ decays, the reconstructed data peak now occurs at approximately 5.75 GeV, while for the true, it occurs later at approximately 14.5 GeV. This is a much larger spread than was seen for the unfiltered data. Both the p_T and $p_{T,\,TRUE}$ also show significant increases.

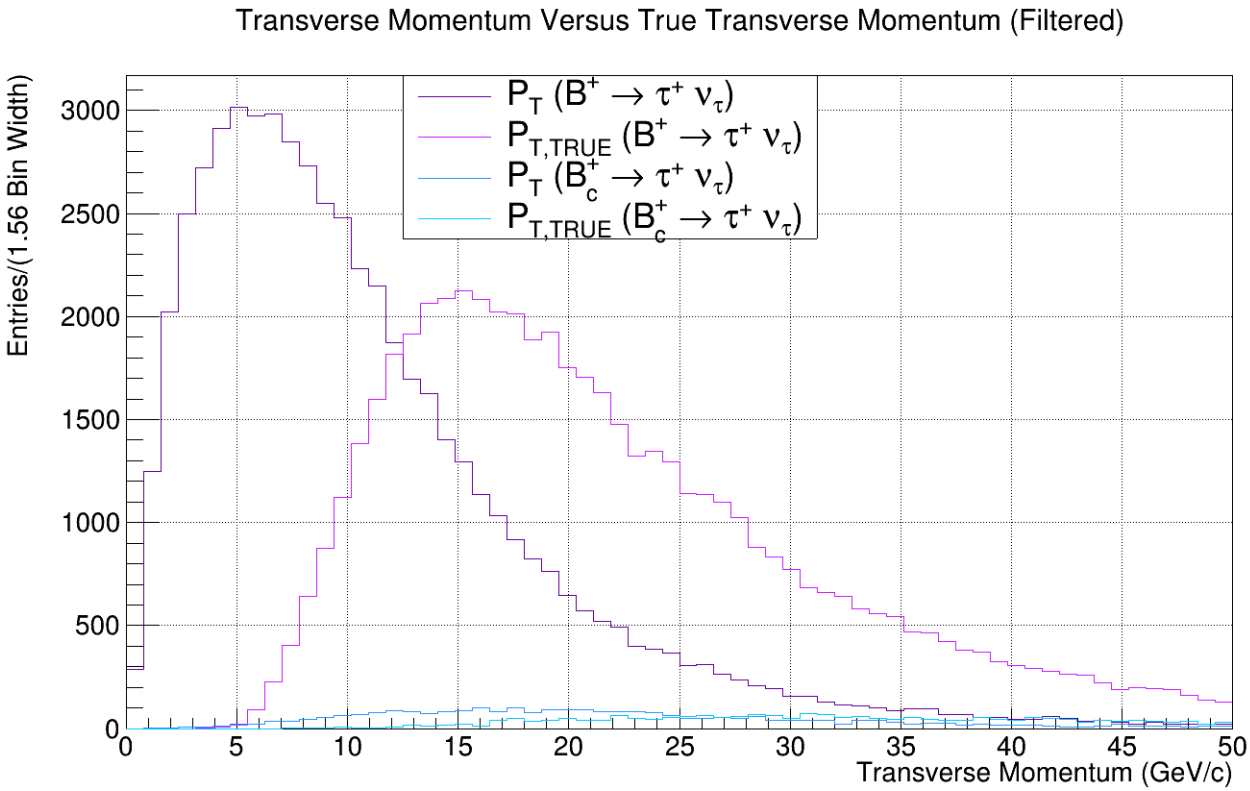

Figure 6.2: The values for the transverse momentum for the B^+ and B_c^+ decays using filtered data.

Figure 6.3 shows the filtered transverse momentum for only B_c^+ decays. The number of entries is much lower than that of its B^+ counterpart, hence the eclipsing phenomenon in Figure 6.2. The B_c^+ decay can decay through both the b-quark and the c-quark; therefore, it has a shorter lifetime than its B^+ counterpart. With a shorter lifetime, the VELO hit requirement will force the B_c^+ decay to have a more considerable momentum to reach the VELO. This results in fewer B_c^+ decays fulfilling the requirement of the filtering process, explaining the eclipsing phenomenon seen in Figure 6.2.

The reconstructed transverse momentum peaks between approximately 16 and 23 GeV for the B_c^+ decays, while the true peaks at approximately 31.75 GeV. The B_c^+ follows the same general trend as the B^+ though it occurs at higher transverse momentum values, thus explaining the high p_T values for the B_c^+ decay.

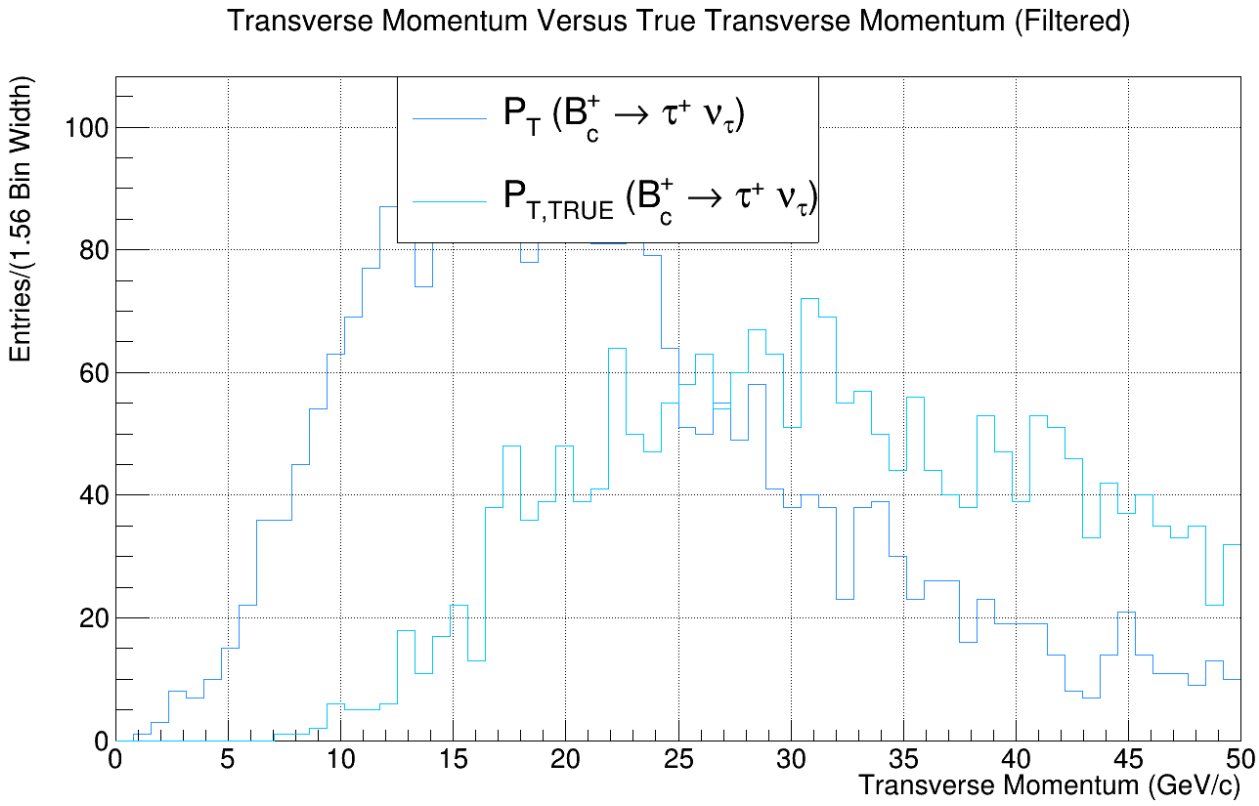

Figure 6.3: The values for the transverse momentum for the B_c^+ decays using filtered data.

Table 6.1 denotes the average transverse momentum values for the p_T and $p_{T,\,TRUE}$ graphs for B^+ and B_c^+ for both the unfiltered and filtered data. Along with the lower transverse momentum peak, the average p_T values for the B^+ and B_c^+ decays are lower than those of the $p_{T,\,TRUE}$. This difference is much larger than the unfiltered, showing that the filtering procedure pushes towards larger transverse momentum values due to the requirement of a hit occurring in the VELO. Therefore, the difference between the p_T and $p_{T,\,TRUE}$ due to the different reconstruction methods also holds for the filtered data.

	Unfiltered Average p_T (GeV)	Filtered Average p_T (GeV)
B^+ p_T	2.80	11.02
B^+ $p_{T,\,TRUE}$	5.32	23.38
B_c^+ p_T	2.96	23.44
B_c^+ $p_{T,\,TRUE}$	5.32	39.99

Table 6.1: Average transverse momentum values for B^+ and B_c^+ for both the p_T and $p_{T,\,TRUE}$ graphs as seen in Figure 6.2 for the filtered data. The average transverse momentum values are taken over a range of 0 to 100 GeV using the piece-wise adjusted f_c/f_u correction in Equation (6.2).

6.2 Weighted Transverse Momentum

The f_c/f_u corrected weight from Equation (4.5) is applied to Figures 6.1 and 6.2 which are repeated with normalized histograms to remove bias. This procedure is applied to both the unfiltered and filtered data to validate the effect that the f_c/f_u correction has on the transverse momentum.

Figure 6.4 shows the histogram for the unfiltered B^+ decay data, however, the unfiltered B_c^+ decay data was corrected using Equation (4.5). The graph was normalized so the data would be on a similar scale. This was done using ROOT's normalization method. Normalization is essential for many reasons; however, two reasons are different units or variables measured at different scales. Here, the f_c/f_u correction weight applied to the B_c^+ decay alters the data, and thus normalization allows any bias to be removed compared to the unweighted B^+ data.

Figure 6.4 graphically represents the transverse momentum of the unfiltered B^+ and B_c^+ decays where the B_c^+ decays have the f_c/f_u correction from Equation (4.5) added. There is only a small discernible difference between Figure 6.1 and 6.4 due to the weighting. It can be seen that the difference in the p_T peak remains the same between the two graphs while a difference in the $p_{T,\,TRUE}$ peak has arisen. Thus, the weighting on the p_T has not caused a discernible difference; however, on the $p_{T,\,TRUE}$ it has.

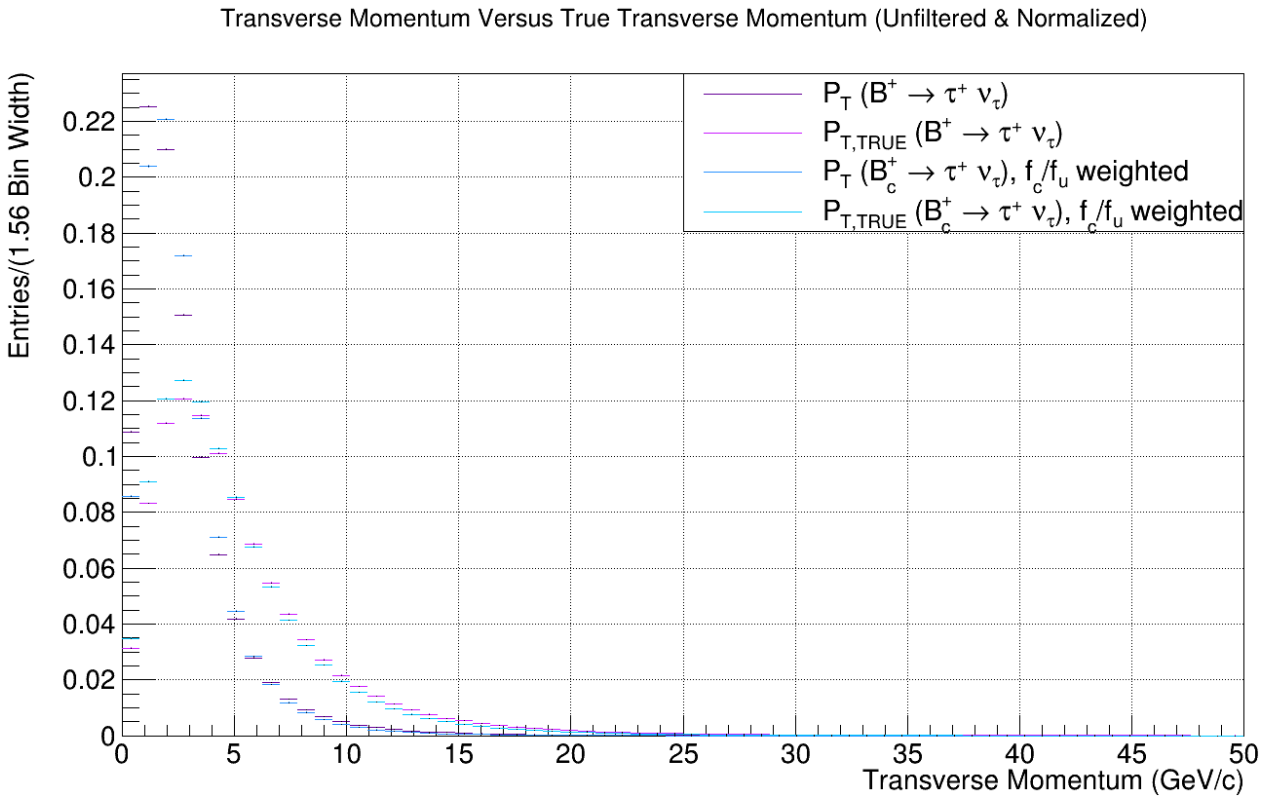

Figure 6.4: The values for the transverse momentum for the B_u^+ and B_c^+ decays using unfiltered data. The B_c^+ decay values are f_c/f_u corrected. All four lines have been normalized.

The average p_T and $p_{T,\,TRUE}$ before and after the f_c/f_u correction are shown in Table 6.2. The differences in the p_T and $p_{T,\,TRUE}$ are 0.16 and 0.46 GeV respectively. Thus, the f_c/f_u correction reduces the p_T and $p_{T,\,TRUE}$ average values. This follows the theory that the f_c/f_u correction causes a decrease as a function of transverse momentum. With the comparison between the original and f_c/f_u corrected unfiltered data discussed, one repeats the analysis for the filtered data.

	Unfiltered	
	Average p_T (GeV)	Weighted Average p_T (GeV)
B^+ p_T	2.80	
B^+ $p_{T,\,TRUE}$	5.32	
B_c^+ p_T	2.96	2.80
B_c^+ $p_{T,\,TRUE}$	5.32	4.87

Table 6.2: Average transverse momentum values for B^+ and B_c^+ for both the p_T and $p_{T,\,TRUE}$ graphs as seen in Figure 6.1 for the unfiltered data respectively. The average transverse momentum values are taken over a range of 0 to 100 GeV using the piece-wise adjusted f_c/f_u correction in Equation (6.2).

Figure 6.5 graphically represents the transverse momentum of the filtered B^+ and B_c^+ decays where the B_c^+ decays have the f_c/f_u correction from Equation (4.5) added. The eclipsing phenomenon seen in Figure 6.2 is no longer present due to the normalization of the individual histograms. This normalization shows that the shapes of the B^+ and B_c^+ transverse and true transverse momentum are similar though they occur at different transverse momentum values. The difference between the B^+ and B_c^+ peaks is approximately 9 GeV for both decays, thus showing a similarity between the shapes.

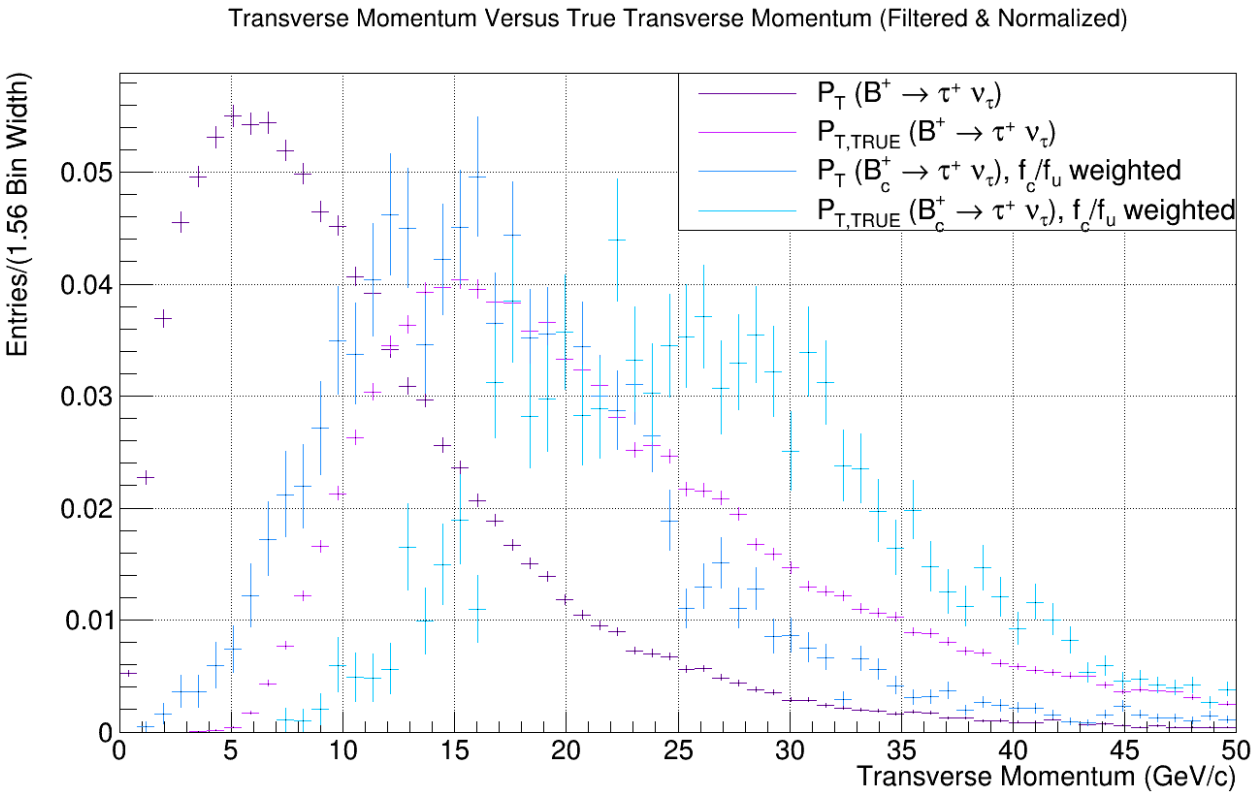

Figure 6.5: The values for the transverse momentum for the B_u^+ and B_c^+ decays using filtered data. The B_c^+ decay values are f_c/f_u corrected. All four lines have been normalized.

Table 6.3, shows the average transverse and true transverse momentum for Figure 6.5. The results follow the same trend as seen previously in Table 6.2 once again showing that the requirement of the hit in the VELO causes a significant change in the average transverse momentum.

	Filtered	
	Average p_T (GeV)	Weighted Average p_T (GeV)
B^+ p_T	11.02	
B^+ $p_{T,\,TRUE}$	23.38	
B_c^+ p_T	23.44	18.39
B_c^+ $p_{T,\,TRUE}$	39.99	29.69

Table 6.3: Average transverse momentum values for B^+ and B_c^+ for the p_T and $p_{T,\,TRUE}$ graph as seen in Figure 6.2 for the filtered data. The average transverse momentum values are taken over a range of 0 to 100 GeV using the piece-wise adjusted f_c/f_u correction in Equation (6.2).

For B_c^+ , which contains the f_c/f_u correction, it can be seen that the average p_T and $p_{T,\,TRUE}$ are increased compared to the unfiltered data. Therefore the VELO requirement increases the transverse and true transverse momentum for both data types. The decrease in the average transverse and true transverse momentum, due to the f_c/f_u correction, remains apparent for the B_c^+ p_T and $p_{T,\,TRUE}$.

One large difference between the unfiltered and filtered data can be seen in the percentage difference. The percentage differences between the average and f_c/f_u corrected average for the p_T and $p_{T,\,TRUE}$ can be seen Table 6.4. The percentage difference between the values can be seen to increase between each respective value, thus showing that the f_c/f_u correction has a larger impact for the $p_{T,\,TRUE}$ compared to the p_T values and a larger impact for the filtered compared to the unfiltered values.

The f_c/f_u correction depends on the value of the B_c^+ decays $p_{T,\,TRUE}$ value, which is on average higher than its p_T counterpart. This explains why the percentage difference is more considerable for the $p_{T,\,TRUE}$ compared to the p_T as the $p_{T,\,TRUE}$ averages are higher than those of the p_T . The same argument holds for the filtered versus unfiltered data.

	Average p_T (GeV)	Weighted Average p_T (GeV)	Percentage Difference
Unfiltered B_c^+ p_T	2.96	2.80	-5.6 %
Unfiltered B_c^+ $p_{T,\,TRUE}$	5.32	4.87	-8.8%
Filtered B_c^+ p_T	23.44	18.39	-24.1%
Filtered B_c^+ $p_{T,\,TRUE}$	39.99	29.69	-29.6%

Table 6.4: Average transverse momentum values for B_c^+ for both the p_T and $p_{T,\,TRUE}$ graphs as seen in Figures 6.1 and 6.2 for the unfiltered and filtered data respectively. The percentage difference between the values are included. The average transverse momentum values are taken over a range of 0 to 100 GeV using the piece-wise adjusted f_c/f_u correction in Equation (6.2).

6.3 Validation of the f_c/f_u Correction

In mathematics, a ratio is used to compare two or more numbers. It is a measurement that shows how large or small a quantity is compared to another. A ratio is therefore taken to investigate the comparison between the B_c^+ and B^+ entries at different transverse momentum values. Determining the different ratios allows for validation to confirm if the f_c/f_u correction is acting as the theory predicts and checking for any discrepancies.

Firstly, the ratio in Equation 6.1 was taken for the unfiltered and filtered data. This ratio aims to validate the results found previously in-regards to the transverse dependence as well as the f_c/f_u correction affecting this dependence.

$$\frac{B_c^+}{B^+} \tag{6.1}$$

6.3.1 Negative Transverse Momentum

The ratio in Equation 6.1 was taken for the unfiltered data up to 100 GeV. In Figure 6.6 it can be seen that the ratio of B_c^+/B^+ became negative at approximately 50 GeV thus signalling an issue with the f_c/f_u correction. The issue lies with the f_c/f_u correction was confirmed by the B_c^+/B^+ uncorrected ratio staying positive. This phenomenon occurs since the B_c^+/B^+ production measurement range is limited.

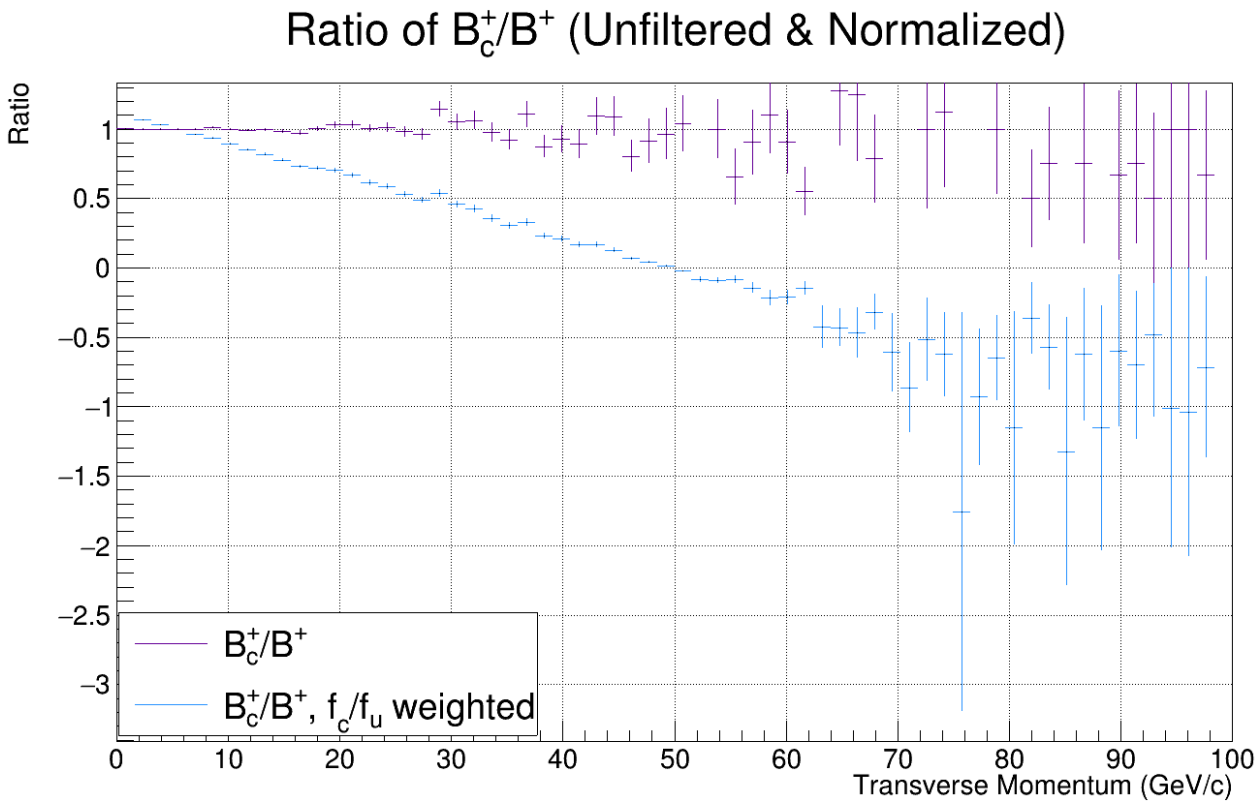

Figure 6.6: Ratio of B_c^+/B^+ for both the original and f_c/f_u corrected B_c^+ using unfiltered data up to 100 GeV. Both lines have been normalized.

To remedy this issue, the f_c/f_u correction was altered to become a piece-wise function which was applied to Equation (4.5). This alteration can be seen in Equation (6.2) where $x_{\text{threshold}}$ denotes the threshold value before the transverse momentum becomes negative and x_{expected} the value of the original f_c/f_u correction at that threshold value. Throughout this research, the values used are 45 GeV and 0.46 for $x_{\text{threshold}}$ and x_{expected} respectively.

$$\text{Equation (4.5)} \quad \frac{f_c}{f_u}(p_T) = 2A[p_1 + p_2(p_T(H_b) - \langle p_T \rangle)]$$

$$\begin{aligned}\text{Piece-Wise Alteration} \quad \frac{f_c}{f_u}(p_T) = (B_c^+\ p_{T,TRUE} > x_{\text{threshold}})(x_{\text{expected}}) \\ + p_{T,TRUE} < x_{\text{threshold}})(2A[p_1 + p_2(p_T(H_b) - \langle p_T \rangle)])\end{aligned} \tag{6.2}$$

6.3.2 Ratio of the f_c/f_u Correction for the Unfiltered and Filtered Data

Figure 6.7, demonstrates the ratio of B_c^+/B^+ (Equation 6.1) with and without the f_c/f_u correction on the B_c^+ for the unfiltered data. With the addition of the f_c/f_u correction on the B_c^+ , it can be seen that the f_c/f_u correction modifies the ratio such that with increasing transverse momentum, the ratio decreases, meaning that the B^+ decay becomes dominant. Thus, the f_c/f_u correction causes transverse momentum to decrease for the B_c^+ decay. This shows a change in the kinematic distribution and validates the transverse momentum dependence as expected from Figure 4.2.

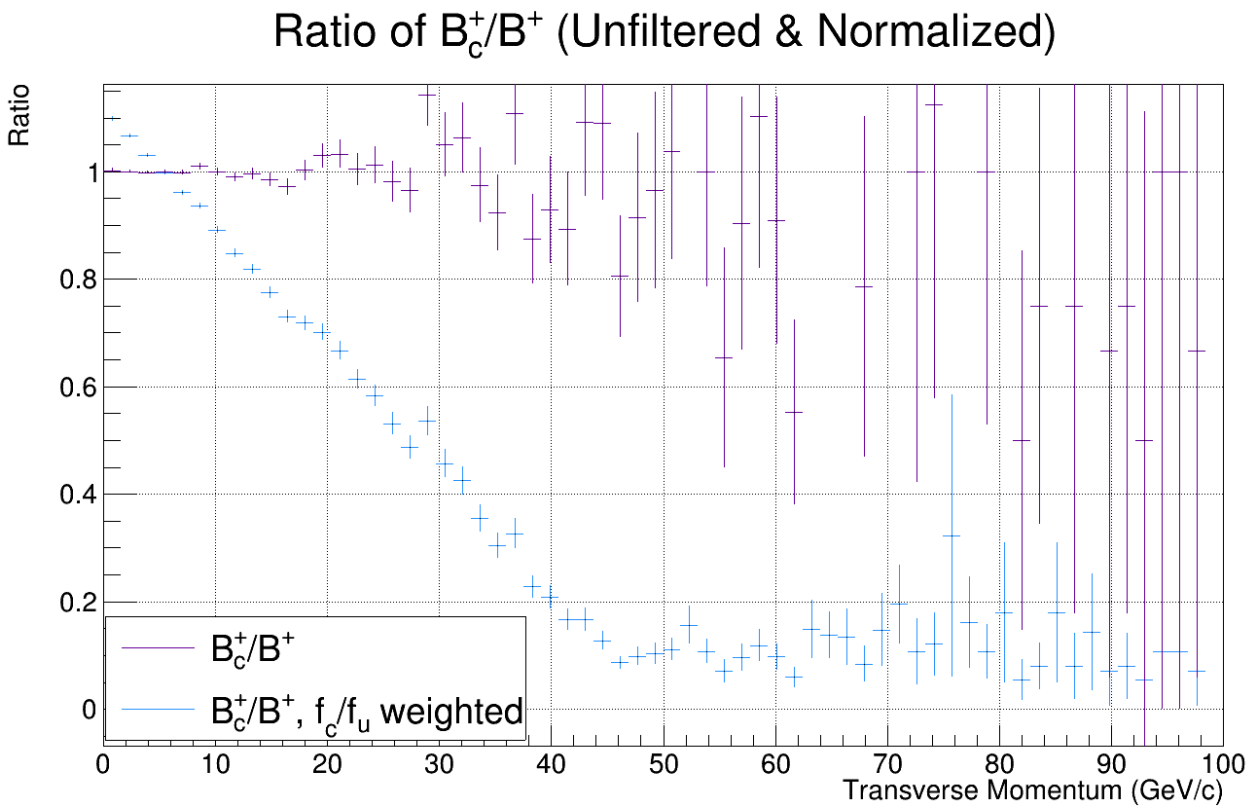

Figure 6.7: Ratio of B_c^+/B^+ for both the original and f_c/f_u corrected B_c^+ using unfiltered data. Both lines have been normalized. Data plotted to 100 GeV to demonstrate the stability due to the piece-wise correction.

With this development of the decreasing ratio as transverse momentum increases, one considers the ratio of B_c^+/B^+ (Equation 6.1) with and without the f_c/f_u correction on the B_c^+ for the filtered data. The filtered data ratio is shown in Figure 6.8. It follows neither of the patterns that the unfiltered data showed. For both the original and the f_c/f_u corrected data, there is an upward trend from approximately 7 to 30 GeV, of which the weighted B_c^+ is seen to be greater than the unweighted. After 30 GeV, the weighted B_c^+ trends slightly downwards while the unweighted B_c^+ trends upwards.

This is to be expected since Figure 6.5 showed that as transverse momentum increased, the B_c^+ decay becomes prevalent. This thus translates into the ratio of B_c^+ / B^+ increasing in favour of B_c^+ at higher transverse momentum values. The f_c/f_u correction on the B_c^+ reduces this dominance due to the dependence of the filtering on the transverse momentum, thus the decrease after that 30 GeV point.

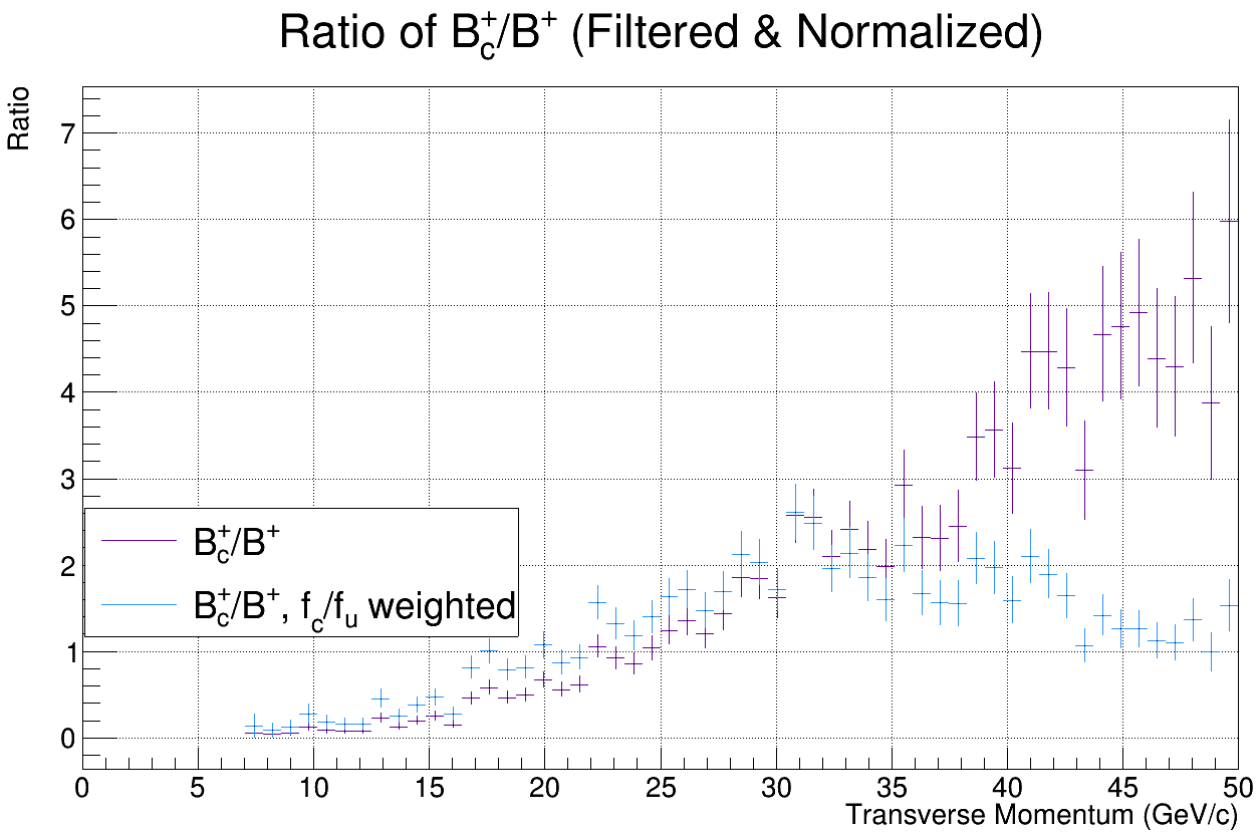

Figure 6.8: Ratio of B_c^+/B^+ for both the original and f_c/f_u corrected B_c^+ using filtered data. Both lines have been normalized.

Figures 6.7 and 6.8, validate the dependence of the filtering on transverse momentum and validate the f_c/f_u correction reducing the dependence of the B^+ / B_c^+ rate. Thus providing a correction for the kinematic difference between the B^+ and B_c^+ decays.

Figure 6.9, demonstrates the ratio of the filtered B_c^+ /unfiltered B_c^+ with and without the f_c/f_u correction. Without the correction, the filtering efficiency for the B_c^+ shows the dominance of filtered data as transverse momentum increases. This is expected due to the difference between filtered and unfiltered data, as previously discussed. The f_c/f_u correction shows the reduction of this trend instead of showing some stability from approximately 20 to 40 GeV rather than an upward or downward trend. This demonstrates the effect that the f_c/f_u correction has on filtering efficiency.

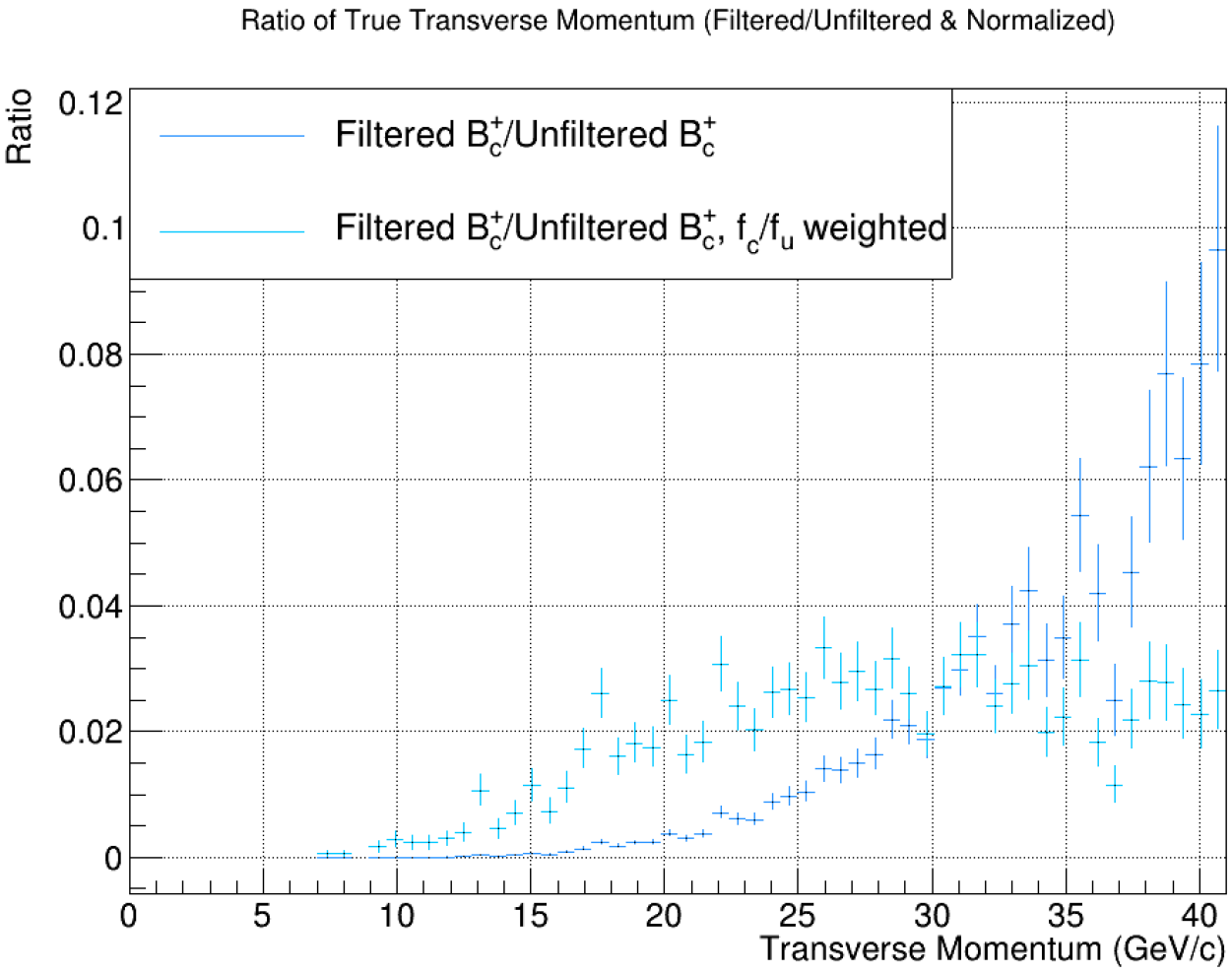

Figure 6.9: Ratio of filtered B_c^+ /unfiltered B_c^+ for both the original and the f_c/f_u corrected samples. Both lines have been normalized both before and after the divide operation occurred.

7

Effect on Filtering Efficiency

With the understanding and validation of the dependence of the filtering on the transverse momentum and the effect of the f_c/f_u correction, this chapter of the research considers the effect that these concepts have on the filtering efficiency of the VELO. The change in filtering efficiency, due to the f_c/f_u correction, is calculated, and then a maximum likelihood estimation fit is used to compare the different efficiencies.

7.1 f_c/f_u Correction Effect on Filtering Efficiency

The f_c/f_u correction applied to the B_c^+ contributes to and alters the data; therefore, one considers its effect on the filtering efficiency. The VELO efficiency arises from the requirement of the hit in the VELO. This efficiency was obtained by taking the average of the efficiencies for all samples, which resulted in a value of 2.9×10^{-4}.

The f_c/f_u corrected VELO efficiency is calculated by taking the ratio of the averages of the filtered and unfiltered weights and multiplying by the VELO efficiency as seen in Equation (7.1).

$$\frac{\text{average of filtered weights}}{\text{average of unfiltered weights}} \times \text{VELO efficiency} \tag{7.1}$$

The results of the VELO efficiency and the corresponding weighted VELO efficiency are given in Table 7.1. It was calculated at thresholds of 45 and 49.8 GeV.

VELO Efficiency	2.9×10^{-4}
f_c/f_u Corrected VELO Efficiency (Threshold at 45 GeV)	9.63×10^{-5}
f_c/f_u Corrected VELO Efficiency (Threshold at 49.8 GeV)	8.70×10^{-5}

Table 7.1: Results for the VELO efficiency and the f_c/f_u corrected VELO efficiency calculated using Equation (7.1). The f_c/f_u corrected VELO efficiency was calculated at thresholds of 45 and 49.8 GeV.

The threshold of 49.8 GeV signifies the highest transverse momentum at which the f_c/f_u correction was naturally positive. It was considered to determine if there was a significant difference between the initial estimate of the 45 GeV threshold.

The f_c/f_u corrected VELO Efficiency was calculated at thresholds of 45 and 49.8 GeV, both of which have a factor of 10^{-5} compared to the factor of 10^{-4} of the VELO efficiency. The 8.70×10^{-5} at a threshold of 49.8 GeV has a 10% percentage difference compared to the 9.63×10^{-5} at a threshold of 45 GeV.

The f_c/f_u corrected VELO Efficiency of 9.63×10^{-5} at the minimal threshold of 45 GeV has a 100% percent difference compared to the 2.9×10^{-4} value for the VELO efficiency. This approximate 1.94×10^{-4} difference between the two values is significant. While the 45 and 49.8 GeV values are arbitrary, the data shows they bound a sensible range.

7.2 Maximum Likelihood on Filtering Efficiency

As shown again below, equation (4.6) explains how the branching and production fractions are influenced by efficiency.

$$N_{\text{fit}}(B_c^+ \to \tau^+\nu_\tau) = N_{\text{data-set}}(B_c^+ \to \tau^+\nu_\tau) \cdot \epsilon_{\text{detector}}(B_c^+ \to \tau^+\nu_\tau)$$

The variable $N_{\text{data-set}}$ can be further broken down as shown in Equation (7.2) where $\mathcal{L}$ denotes the luminosity of the detector, σ_{pp} the cross section of the proton-proton beam, f_c the production fraction, and $\mathcal{B}$ the branching fraction.

$$N_{\text{data-set}} = \mathcal{L} \cdot \sigma_{pp} \cdot f_c \cdot \mathcal{B}(B_c^+ \to \tau^+\nu_\tau) \tag{7.2}$$

The values for the variables are $10\ \text{fb}^{-1}$, 0.65, and 1.82×10^{-3} for $\mathcal{L}$, $\sigma_{pp} \cdot f_c$, and $\mathcal{B}(B_c^+ \to \tau^+\nu_\tau)$ respectively. These values are from *Feasibility study of the branching fraction measurements of* $B_c^+ \to \tau^+\nu_\tau$ *and* $B^+ \to \tau^+\nu_\tau$ *at LHCb* [23] where the combination of $\sigma_{pp} \cdot f_c$ represents the production cross section.

A two-dimensional fit is required to further study the effect of the corrected VELO filtering efficiency. To create a two-dimensional fit, a maximum likelihood (ML) fit is used to extract the signal yield from a dataset which contains the $B_c^+ \to \tau^+(\pi^+\pi^+\pi^-\overline{\nu_\tau})\nu_\tau$ signal, the $B^+ \to \tau^+\nu_\tau$ signal, and the signal of the most dangerous background, the $B^+ \to D^0\pi^+\pi^+\pi^-$. The MLE fit uses the corrected mass and variables from multivariate analysis (MVA).

Separating the signal from the background is done using MVA techniques. This involves formulating mathematical functions of a number of input variables, such as invariant mass, which may, on its own, contribute to varying degrees of signal-to-background separation [24]. These procedures generate output variables that best distinguish the signal from the background. These output variables can be viewed as scores or rankings of events based on their signal- or background-like characteristics. Using this MVA score and the events simulated by RapidSim, a maximum likelihood and fit are simulated as would be done with real detector data. More information on this MVA and MLE fit can be found in the paper *Improving the sensitivity study of* $B_c^+ \to \tau^+\nu_\tau$ *at the LHCb detector by rejecting the three most dangerous background modes* [25].

Table 7.2*, shows the results of the MLE fit using the MVA score for both the VELO efficiency and the f_c/f_u corrected VELO efficiency.

	VELO Efficiency 2.9×10^{-4}	f_c/f_u VELO Efficiency 9.63×10^{-5}	Difference	Ratio
Signal Yield	3358	1026	-2332	31%
Error on Signal Yield	132.7	105.0	-27.7	79%
Total Uncertainty	4.0%	10.2%	6.3%	
Statistical Uncertainty	58.0	32.0	-25.9	55%
Systematic Uncertainty	119.4	100.0	-19.4	84%

Table 7.2: Results for the VELO efficiency compared to the f_c/f_u corrected VELO efficiency for the signal yield, the error on the signal yield, the total uncertainty, statistical uncertainty, and the systemic uncertainty. The systemic uncertainty is calculated by taking the square root sum difference of the error on the signal yield and the statistical uncertainty.

The f_c/f_u correction on the VELO efficiency (9.63×10^{-5}) has a difference of 1.94×10^{-4} with respect to the original. This causes a difference of 2332 in terms of signal yield, which shows that the signal yield is decreased by approximately a factor of three due to the f_c/f_u correction. The errors on the signal yield are reduced from 133 to 105. The statistical uncertainty is reduced from 58 to 32 and the systematic uncertainty from 119 to 100, thus demonstrating that the resulting error increases with the decrease in signal yield. While the singular uncertainties are slightly lower, the overall signal yield is smaller by a factor of three, and thus the errors have a larger effect. One considers the fits for the resulting data to better understand this decrease in signal yield but increase in uncertainty.

The maximum likelihood fits using an MVA for both the VELO efficiency and the corrected VELO efficiency are shown in Figures 7.1 (a) and 7.1 (b), respectively. Figure 7.1 (a) shows a distinct difference between the different curves. After 6 GeV/c^2 the B_c^+ decay trends are higher than the $B^+ \to \tau^+\nu_\tau$ decay, which demonstrates a possibility to distinguish the B_c^+ signal from the $B^+ \to \tau^+\nu_\tau$ background. The most dangerous background, $B^+ \to D^0\pi^+\pi^+\pi^-$, also falls below the B_c^+ signal after 6 GeV/c^2 which suggests a possibility to distinguish the signal and backgrounds.

In Figure 7.1 (b), the distinction between the curves becomes smaller, with the difference between the B_c^+ and $B^+ \to \tau^+\nu_\tau$ curves becoming negligible. This is due to the B_c^+ decay curve becoming lower on average. This is seen explicitly at the peak and the end of the curve, which are approximately half of their original values, thus showing the impact that the correction has on affecting the transverse momentum, which was discussed previously. The propagation of the lower B_c^+ values is seen by, the lower values at the end of the generated data and total fit curves. The $B^+ \to \tau^+\nu_\tau$ and $B^+ \to D^0\pi^+\pi^+\pi^-$ curves remain the same as in Figure 7.1 (a) as the B_c^+ has no effect on them.

The decrease of the B_c^+ decay curve results in little to no difference between the tails of the B_c^+ and $B^+ \to \tau^+\nu_\tau$ decay curves. Thus it becomes much harder to distinguish the signal from the background compared to the situation in Figure 7.1 (a); however, the MVA use still allows for potential separation.

*MVA and the corresponding MLE fit generated by Pietro Albanese. More information on this MVA and MLE fit can be found in the paper *Improving the sensitivity study of $B_c^+ \to \tau^+\nu_\tau$ at the LHCb detector by rejecting the three most dangerous background modes* [25].

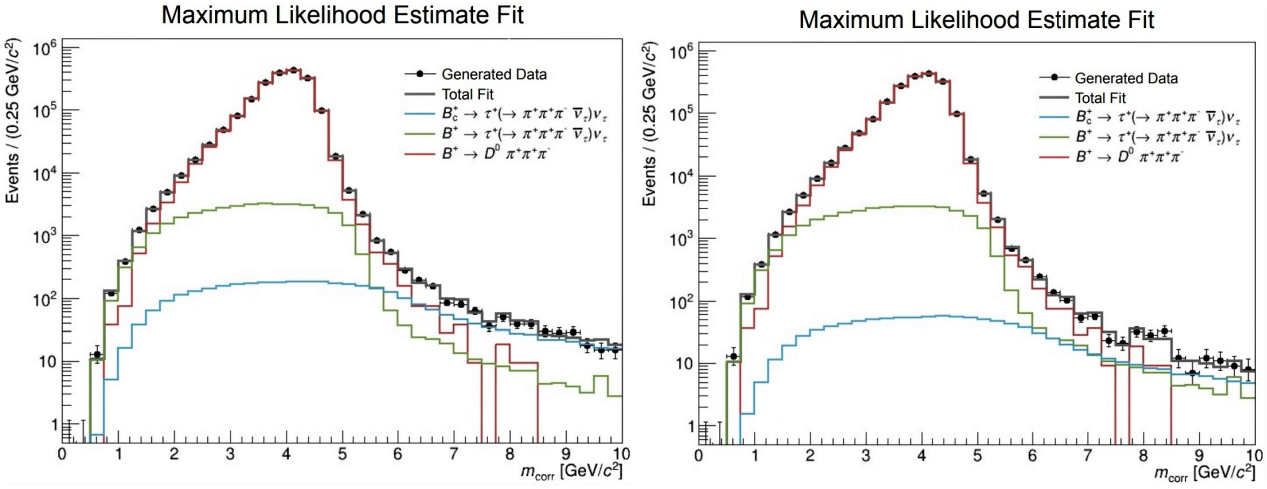

(a) Maximum likelihood Hit for the VELO filtering efficiency value of 2.9×10^{-4}.

(b) Maximum likelihood Hit for the corrected VELO filtering efficiency value of 9.63×10^{-5}.

Figure 7.1: Maximum likelihood Hit for the VELO filtering efficiency and the corrected VELO efficiency. The fits are without any cuts on the invariant mass.

While this correction for the difference in the B_c^+ and B^+ kinematics causes a decrease in signal yield, the Maximum likelihood estimation fit results signify that differentiation between signal and background is still possible. The decrease in signal yield does lead to an increase in uncertainty. Thus the potential for differentiating signal from the background is still possible, although harder than before.

8 Discussion

This research has mainly focused on theoretical learning and data analysis through concepts such as branching and production fractions, applying a f_c/f_u correction to reduce the dependence of the filtering on the transverse momentum, and validating these results on a simulation. Finally, the research investigated the potential effect of the f_c/f_u correction on the VELO filtering efficiency. This discussion expands on the relevance of these results and leads to a discussion on possible improvements for the future of this study.

8.1 B_c^+ Meson Kinematics

8.1.1 Transverse & True Transverse Momentum and Unfiltered & Filtered Data

The study of the B_c^+ meson kinematics showed essential differences between transverse and true transverse momentum and the unfiltered and filtered data. The important distinction between the transverse and true transverse momentum was the differing methods of smearing. This led to approximately 2.44 GeV difference between the p_T and $p_{T,\,TRUE}$. This effect occurs because the p_T is reconstructed from the pions following the final state of the $B_c^+ \to \tau^+(\pi^+\pi^+\pi^-\overline{\nu_\tau})\nu_\tau$ decay, which emulates the resolution on the momentum. However, the p_T does not include the missing neutrinos, and therefore, there is lost momentum. In contrast, the $p_{T,\,TRUE}$ is generated using FONLL and the p_T histogram.

A larger discrepancy was seen between the unfiltered and filtered data with Table 6.1 showing average differences of 8.22 and 18.06 GeV for the B^+ p_T and $p_{T,\,TRUE}$ respectively, and 20.48 and 34.67 GeV for the B_c^+ p_T and $p_{T,\,TRUE}$ respectively. This demonstrates that the requirement of a hit occurring in the VELO substantially changes the situation.

Mesons must travel a minimum distance away from the beam axis, in the transverse direction, to come across a sensor since the VELO sensors for the improved detector utilized in Run 3 will sit roughly 5.1 mm from the beam axis. The B_c^+ meson has a shorter lifetime compared to the B^+ . This is due to the possibil-

ity for the B_c^+ meson to decay through both the b-quark and c-quark. This shorter lifetime means that the filtering requirement will have a more substantial effect on the B_c^+ meson by requiring higher transverse momentum values. The cross-section for the generation of heavy particles also depends on transverse momentum, hence showing the importance of understanding transverse momentum dependencies.

8.1.2 f_c/f_u Correction for Kinematic Differences

To correct for the kinematic differences between the B_c^+ and B^+ mesons, a f_c/f_u correction was applied through the use of Equation (4.5). However, due to the negative transverse momentum problem which was discovered in section 6.3.1, the f_c/f_u correction was transformed into a piece-wise function, as seen in Equation (6.2), which used 45 GeV as the threshold. This alteration forced the f_c/f_u correction to adjust past the threshold.

The prominent difference caused by the f_c/f_u correction was a decrease as a function of the transverse momentum. To validate the correction and its results, the ratio of B_c^+/B^+ was taken for the unfiltered and filtered data. For the unfiltered B_c^+/B^+ ratio without the correction, the ratio remains approximately around 1 while it trends steadily downwards with the f_c/f_u correction. This steady downward trend shows that the B^+ decay dominates as transverse momentum increases, showing a kinematic distribution change.

The filtered ratio of B_c^+/B^+ showed an initial steady increase for both the ratio and the corrected ratio until approximately 30 GeV. Past this point, the uncorrected ratio steadily increased while the corrected ratio followed an opposite trend. Thus showing once again a steady downwards trend in which B^+ dominates as transverse momentum increases, showing a change in the kinematic distribution.

The filtered efficiency graph shows dominance when the B_c^+ is corrected between approximately 10 and 28 GeV. The ratio of the filtered B_c^+ divided by the unfiltered B_c^+ showed a steadily increasing trend for the uncorrected data. When the f_c/f_u correction was added, it showed an initially higher trend which remained somewhat stable until decreasing slightly around 30 GeV. After 30 GeV, the uncorrected data becomes dominant while the corrected data demonstrates the same downward trend seen in previous graphs. Thus once again validating a change in the kinematic distribution.

8.2 Effect on Filtering Efficiency

With the f_c/f_u correction validated, it became important to consider the effects of the correction on the filtering efficiency. A new efficiency value was found by determining the difference between the average filtered and unfiltered correction weights and multiplying by the original VELO efficiency value of 2.9×10^{-4}. At the 45 GeV threshold, this value was found to be 9.63×10^{-5} which is 1.94×10^{-4} lower than the original VELO efficiency.

To determine the effects that a lower efficiency has on signal yield and uncertainty, a maximum likelihood estimation was used, which included multivariate analysis. The maximum likelihood results showed that the lower efficiency caused the signal yield to decrease by a factor of three while also increasing the total uncertainty from 4% to 10.2%.

Figures 7.1 (a) and 7.1 (b) demonstrated the lower signal yield. However, more importantly, the figures showed that the lower signal yield of the B_c^+ decay causes it to become harder to distinguish the signal from

the background. Due to the approximate 10% total uncertainty, there is still a possibility for the signal and background to be distinguished, but this should be validated in further research.

The significance of the result can be estimated through $N - S \cdot \sigma_N = 0$ where N is the number of signal yield, S the significance, and σ_N the error on the signal yield. The VELO efficiency results in a significance of approximately 25σ while for the f_c/f_u corrected efficiency, this significance decreases to 10σ. The significance measures how likely background modes are to act as fake signal events; this decrease in significance thus implies a higher chance of this occurring. While this complicates signal and background differentiation, the significance value above the 5σ threshold suggests that differentiation is still possible.

8.3 Future Improvements

A limiting factor of this research is the short timeline. A substantial amount of time was invested into the initial learning of the topics involved in this research. Thus moving into the future, there are many topics that should be considered for further research.

Another consideration is the negative transverse momentum that was discovered in section 6.3.1. This effect of the transverse momentum becoming negative above 50 GeV with the f_c/f_u correction is something that should be investigated more in-depth. The negative transverse momentum occurred since the B_c^+ , and B^+ production measurement range is limited.

A major problem in experimental high-energy physics is how to distinguish signal from background. This is resolved through the use of multivariate analysis (MVA), which is a group of statistical analytic techniques that examine numerous measurements on the object under study simultaneously. The maximum likelihood fit showed a decrease in signal but an increase in uncertainty. Future research should consider whether or not the signal is still separable from the background due to the higher uncertainty.

Possibly sources of uncertainty come from the f_c/f_u correction weighting and the branching fraction measurements. The f_c/f_u correction has its own uncertainty, which is then propagated through the measurements, thus affecting the weights applied. This then once again propagates through into the efficiency changes. The f_c/f_u correction is also considered to be the number of B_c^+ /bp mesons, which is determined with a limited precision of approximately 25%, which comes from the uncertainty on the branching fraction of the $B_c^- \to J/\psi\mu^-\overline{\nu_\mu}$. Therefore any future calculations on the branching fraction would be limited by this 25% uncertainty. Future improvements on the f_c/f_u measurement would therefore be helpful.

9
Conclusion

A potent approach to test lepton flavour universality in the Standard Model is the examination of $b \to c l \nu$ transitions such as occurs in the $B_c^+ \to \tau^+(\pi^+\pi^+\pi^-\overline{\nu_\tau})\nu_\tau$ decay. The $B_c^+ \to \tau^+(\pi^+\pi^+\pi^-\overline{\nu_\tau})\nu_\tau$ is very difficult to observe and precisely characterize its features at a hadron collider. This is because a significant amount of energy is missing from the final state, the centre-of-mass energy of the $b\bar{b}$ creation process is unknown, there are many backgrounds resulting from the hadronic environment's numerous primary vertices, and there isn't a reconstructible B_c^+ decay vertex. If lepton flavour universality is broken, this would be an unmistakable sign of new physics.

At a hadron collider, such as the Large Hadron Collider, the presence of at least one undiscovered neutrino makes it challenging to accurately measure the branching fraction of a b-hadron decaying leptonically such as $B_c^+ \to \tau^+(\pi^+\pi^+\pi^-\overline{\nu_\tau})\nu_\tau$. To provide complementary experimental challenges in the two decay modes, $B_c^+ \to \tau^+(\pi^+\pi^+\pi^-\overline{\nu_\tau})\nu_\tau$ and $B^+ \to \tau^+\nu_\tau$, the tau lepton can be recreated in its hadronic $\tau^+ \to \pi^+\pi^+\pi^-\overline{\nu_\tau}$ final state. A precise measurement of the tau lepton's decay vertex is possible thanks to the existence of three discernible pion tracks coming from the particle.

This research focused on understanding the theoretical differences between transverse and true transverse momentum and the difference between unfiltered and filtered data. Measurements of the $B_c^+ \to \tau^+\nu_\tau$ decay type are challenging. This is due to the neutrinos involved in the $B_c^+ \to \tau^+(\pi^+\pi^+\pi^-\overline{\nu_\tau})\nu_\tau$ decay, which cannot be detected; consequently, the B_c^+ decay vertex cannot be reconstructed. A B-tracking tool is used to infer the direction of the B_c^+ meson, which measures hits of the B_c^+ meson in the Vertex Locator sub-detector rather than its decay products. Chapter 6 concluded that the requirement of a hit in the VELO, which is the filtering requirement, requires B_c^+ mesons to have higher transverse momentum values to reach the VELO. This effect is not as strong for the B^+ due to its longer lifetime. The chapter also concluded that the f_c/f_u correction for the difference between the B_c^+ and B^+ kinematics caused a decrease as a function of the transverse momentum, meaning a change in the kinematic distribution

occurred. This was then validated through the use of ratio plots.

The change in the kinematic distribution and its effects on the filtering efficiency decreased from 2.9×10^{-4} to 9.64×10^{-5}. Using a maximum likelihood with variables such as the corrected mass from a multivariate analysis, a two-dimensional fit demonstrated that change in efficiency resulted in the signal yield decreasing by a factor of three. Figures 7.1 (a) and 7.1 (b) showed that the decrease in signal yield makes it more difficult to distinguish the signal from background. An increase in the total uncertainty accompanied the decrease in signal yield. The total uncertainty is approximately 10%, so there is potentially still an option to distinguish the signal and background. Therefore, future research should consider whether the signal is distinguished from the background.

In conclusion, **the application of the f_c/f_u correction to account for kinematic differences between the B_c^+ and B^+ mesons results in a decrease in efficiency and signal yield by a factor of three and a corresponding increase in total uncertainty from 4% to 10%.** Thus the signal and background become harder to separate. The decrease in the significance from 25σ to 10σ also suggests that the background is more likely to mimic signal events and thus further complicate the differentiation. Due to the 10σ being above the 5σ threshold, differentiation is still possible, though future studies of the f_c/f_u measurement will be a crucial factor.

Bibliography

[1] Conseil Européen pour la Recherche Nucléaire. *LHCb*. URL: https://home.cern/science/experiments/lhcb.

[2] Jan IJsbrand Rol. *b-Meson Tracking at LHCb: a Feasibility Study*.

[3] N. A. Jelley. *Fundamentals of Nuclear Physics*. Cambridge University Press, 1990. DOI: 10.1017/CBO9781139167758.

[4] Kristof De Bruyn. "Searching for Penguin Footprints: Towards High Precision CP Violation Measurements in the B Meson Systems (CP en B cursief)". PhD thesis. Vrije U., Amsterdam, Vrije U., Amsterdam, Apr. 2015.

[5] Elise Le Boulicaut and Valerie Buxbaum on behalf of the ATLAS Collaboration. *ATLAS Cheat Sheets*. URL: https://atlas.cern/Resources/Cheat-sheets.

[6] CERN Daniel Dominguez. *Infographics gallery*. URL: https://home.cern/resources/image/physics/infographics-gallery.

[7] F. Englert and R. Brout. "Broken Symmetry and the Mass of Gauge Vector Mesons". In: *Phys. Rev. Lett.* 13 (1964). Ed. by J. C. Taylor, pp. 321–323. DOI: 10.1103/PhysRevLett.13.321.

[8] Peter W. Higgs. "Broken Symmetries and the Masses of Gauge Bosons". In: *Phys. Rev. Lett.* 13 (1964). Ed. by J. C. Taylor, pp. 508–509. DOI: 10.1103/PhysRevLett.13.508.

[9] Roel Aaij et al. "Test of lepton universality in beauty-quark decays". In: *Nature Phys.* 18.3 (2022), pp. 277–282. DOI: 10.1038/s41567-021-01478-8. arXiv: 2103.11769 [hep-ex].

[10] Yasmine Sara Amhis et al. "Averages of b-hadron, c-hadron, and τ-lepton properties as of 2018". In: *Eur. Phys. J.* C81 (2021). updated results and plots available at https://hflav.web.cern.ch/, p. 226. DOI: 10.1140/epjc/s10052-020-8156-7. arXiv: 1909.12524 [hep-ex].

[11] Roel Aaij et al. "Measurement of the ratio of branching fractions $\mathcal{B}(\bar{B}^0 \to D^{*+}\tau^-\bar{\nu}_\tau)/\mathcal{B}(\bar{B}^0 \to D^{*+}\mu^-\bar{\nu}_\mu)$". In: *Phys. Rev. Lett.* 115.11 (2015). [Erratum: Phys.Rev.Lett. 115, 159901 (2015)], p. 111803. DOI: 10.1103/PhysRevLett.115.111803. arXiv: 1506.08614 [hep-ex].

[12] R. Aaij et al. "Measurement of the ratio of branching fractions $\mathcal{B}(B_c^+ \to J/\psi\tau^+\nu_\tau)/\mathcal{B}(B_c^+ \to J/\psi\mu^+\nu_\mu)$". In: *Phys. Rev. Lett.* 120.12 (2018), p. 121801. DOI: 10.1103/PhysRevLett.120.121801. arXiv: 1711.05623 [hep-ex].

[13] Conseil Européen pour la Recherche Nucléaire. *The CERN accelerator complex*. URL: https://panoramas-outreach.cern.ch/index.html.

[14] A. Augusto Alves Jr. et al. "The LHCb Detector at the LHC". In: *JINST* 3 (2008), S08005. DOI: 10.1088/1748-0221/3/08/S08005.

[15] Conseil Européen pour la Recherche Nucléaire. *LHCb upgrade during LS2*. URL: https://home.cern/press/2022/LHCb-upgrades-LS2.

[16] LHCb Collaboration. "LHCb Tracker Upgrade Technical Design Report". In: (Feb. 2014).

[17] G. A. Cowan, D. C. Craik, and M. D. Needham. "RapidSim: an application for the fast simulation of heavy-quark hadron decays". In: *Comput. Phys. Commun.* 214 (2017), pp. 239–246. DOI: 10.1016/j.cpc.2017.01.029. arXiv: 1612.07489 [hep-ex].

[18] LHCb Starterkit. *LHCb data flow in Run 3*. URL: https://lhcb.github.io/starterkit-lessons/first-analysis-steps/dataflow-run3.html.

[19] Roel Aaij et al. "Measurement of the B_c^- meson production fraction and asymmetry in 7 nd 13 TeV pp collisions". In: *Phys. Rev. D* 100.11 (2019), p. 112006. DOI: 10.1103/PhysRevD.100.112006. arXiv: 1910.13404 [hep-ex].

[20] R. Brun and F. Rademakers. "ROOT: An object oriented data analysis framework". In: *Nucl. Instrum. Meth. A* 389 (1997). Ed. by M. Werlen and D. Perret-Gallix, pp. 81–86. DOI: 10.1016/S0168-9002(97)00048-X.

[21] root.cern. *About ROOT*. URL: https://root.cern/about/.

[22] Matteo Cacciari et al. "Theoretical predictions for charm and bottom production at the LHC". In: *JHEP* 10 (2012), p. 137. DOI: 10.1007/JHEP10(2012)137. arXiv: 1205.6344 [hep-ph].

[23] Jelte Rinus de Jong. *Feasibility study of the branching fraction measurements of $B_c^+ \to \tau^+\nu_\tau$ and $B^+ \to \tau^+\nu_\tau$ at LHCb*.

[24] Morad Aaboud et al. "Search for the standard model Higgs boson produced in association with top quarks and decaying into a $b\bar{b}$ pair in pp collisions at $\sqrt{s}$ = 13 TeV with the ATLAS detector". In: *Phys. Rev. D* 97.7 (2018), p. 072016. DOI: 10.1103/PhysRevD.97.072016. arXiv: 1712.08895 [hep-ex].

[25] Pietro Albanese. *Improving the sensitivity study of $B_c^+ \to \tau^+\nu_\tau$ at the LHCb detector by rejecting the three most dangerous background modes*.